Structural and functional properties of a magnesium transporter of the SLC11/NRAMP family

Karthik Ramanadane[1], Monique S. Straub[1], Raimund Dutzler[1*] and Cristina Manatschal[1*]

[1]Department of Biochemistry, University of Zurich, Winterthurerstrasse 190, 8057 Zurich, Switzerland.

*For correspondence: dutzler@bioc.uzh.ch (RD), c.manatschal@bioc.uzh.ch (CM)

Abstract

Members of the ubiquitous SLC11/NRAMP family catalyze the uptake of divalent transition metal ions into cells. They have evolved to efficiently select these trace elements from a large pool of Ca^{2+} and Mg^{2+}, which are both orders of magnitude more abundant, and to concentrate them in the cytoplasm aided by the cotransport of H^{+} serving as energy source. In the present study, we have characterized a member of a distant clade of the family found in prokaryotes, termed NRMTs, that were proposed to function as transporters of Mg^{2+}. The protein transports Mg^{2+} and Mn^{2+} but not Ca^{2+} by a mechanism that is not coupled to H^{+}. Structures determined by cryo-EM and X-ray crystallography revealed a generally similar protein architecture compared to classical NRAMPs, with a restructured ion binding site whose increased volume provides suitable interactions with ions that likely have retained much of their hydration shell.

Introduction

Divalent cations constitute important factors in numerous biological processes and they are thus essential nutrients that need to be imported into cells in the required amounts. From a chemical perspective, we distinguish the alkaline earth metals Ca^{2+} and Mg^{2+} from transition metal ions such as Fe^{2+} and Mn^{2+}, which show distinct properties owing to their size and electronic structure. As major constituent of bone, Ca^{2+} has to be taken up by vertebrates in high amount. Although its largest part is immobilized within the body, free Ca^{2+} is present in the extracellular medium in low millimolar concentrations. In contrast, cytoplasmic Ca^{2+} serves as second messenger and its distribution in the cell thus requires tight control (Carafoli and Krebs, 2016). Mg^{2+} on the other hand is a ubiquitous ligand of nucleotides and nucleic acids (de Baaij et al., 2015; Maguire and Cowan, 2002). Despite the similar extracellular concentration, its abundance in the cytoplasm is several orders of magnitude higher compared to Ca^{2+}. In their interaction with other molecules, these alkaline earth metal ions are coordinated by electronegative hard ligands, preferentially oxygens, which compensate their positive charges by either full or partial countercharges (Carafoli and Krebs, 2016; Payandeh et al., 2013). In contrast to Ca^{2+} and Mg^{2+}, which both constitute minor elements in the human body, transition metals are trace elements that are found at much lower concentration as they are required for specialized processes. Transition metals are distinguished by their incompletely filled d-orbitals. This property permits coordinative interactions with soft ligands containing free electron pairs and allows them to change their oxidation state, which makes them important cofactors in redox reactions. The transition metal ion Fe^{2+} plays a central role in oxygen transport and, together with Mn^{2+}, it is a cofactor of enzymes catalyzing redox reactions. Due to their low abundance in the extracellular environment, the uptake of transition metals has thus to proceed with high selectivity to prevent competition with several orders of magnitude more

43 abundant alkaline earth metals, which would prohibit their efficient accumulation. This challenge
44 is overcome by specific transmembrane transport proteins, which catalyze the accumulation of
45 transition metal ions inside cells. Among these proteins, members of the SLC11/NRAMP family
46 play an important role. They are expressed in all kingdoms of life where they facilitate the
47 transmembrane transport of different transition metal ions by a secondary active process that
48 involves the cotransport of H^+ as energy source (Courville et al., 2006; Nevo and Nelson, 2006).
49 In animals, these proteins are used for the transport of Fe^{2+} (Montalbetti et al., 2013), whereas in
50 prokaryotes the primary substrate is Mn^{2+} (Makui et al., 2000). Besides the transport of both
51 transition metals, plant NRAMPs are also involved in detoxification processes by transporting
52 noxious metal ions such as Cd^{2+} (Huang et al., 2020a).

53 The transport properties of SLC11/NRAMP proteins have been investigated in numerous
54 functional studies (Gunshin et al., 1997; Mackenzie et al., 2006; Makui et al., 2000), supported by
55 the structures of prokaryotic transporters determined in different conformations (Bozzi et al.,
56 2016b; Bozzi et al., 2019b; Ehrnstorfer et al., 2014; Ehrnstorfer et al., 2017). With respect to its
57 fold, the family is distantly related to other secondary active transporters that include the amino-
58 acid transporter LeuT (Ehrnstorfer et al., 2014; Yamashita et al., 2005), although there is little
59 relationship on a sequence level, SLC11/NRAMP structures provide detailed insight into substrate
60 preference and transport mechanisms. Characterized family members show an exquisite selectivity
61 for transition metals over alkaline earth metal ions, but they poorly discriminate between transition
62 metals (Ehrnstorfer et al., 2014; Gunshin et al., 1997). This is accomplished by a conserved ion
63 binding site that is located in the center of the protein (Ehrnstorfer et al., 2014). Several residues
64 coordinate the largely dehydrated metal ion with hard, oxygen-containing ligands, which would
65 equally well interact with other divalent cations. Additionally, the site allows interaction with the

66 free electron pair of the thioether group of a conserved methionine residue, which serves as soft
67 ligand that permits coordinative interactions with transition metal- but not alkaline earth metal ions
68 (Ehrnstorfer et al., 2014). The mutation of this methionine to alanine in one of the bacterial
69 homologues had a comparably small effect on transition metal ion transport but instead converted
70 Ca^{2+} into a transported substrate, which emphasizes the role of the residue in conferring ion
71 selectivity (Bozzi et al., 2016a).

72 Although, throughout kingdoms of life, the majority of SLC11/NRMP transporters share similar
73 functional properties, there are few family members that were described to transport with distinct
74 substrate preference. Among these family members are prokaryotic proteins, termed NRAMP-
75 related magnesium transporters (NRMTs), that were identified as uptake systems for Mg^{2+}. In the
76 bacterium *Clostridium acetobutylicum*, the prototypic NRMT (CabNRMT) has permitted growth
77 at limiting Mg^{2+} concentrations, even in absence of any alternative transport pathways (Shin et al.,
78 2014). The altered substrate preference is remarkable since, owing to its small ionic radius and the
79 consequent high charge density, the interaction of Mg^{2+} with its surrounding solvent is unusually
80 strong, which makes the dehydration of the ion energetically costly and thus requires unique
81 features for its transport (Chaudhari et al., 2020; Maguire and Cowan, 2002). The uptake of Mg^{2+}
82 into cells is thus accomplished by few selective transport systems (Payandeh et al., 2013) that
83 include the bacterial proteins CorA (Lunin et al., 2006), CorC (Huang et al., 2021), MgtE (Tanaka
84 et al., 2007) and their eukaryotic homologues (Schaffers et al., 2018; Schweigel-Rontgen and
85 Kolisek, 2014), the TRP channel TRPM7 (Huang et al., 2020b) and Mg^{2+}-selective P-type pumps
86 (Maguire, 1992). In the present study we became interested in the mechanism of Mg^{2+} transport
87 by SLC11 proteins and we thus set out to investigate the functional and structural basis of this
88 process by combining transport experiments with structural studies. We identified a biochemically

89 well-behaved NRMT, which allowed us to characterize its transport behavior using *in vitro*
90 transport experiments. Structure determination by cryo-electron microscopy and X-ray
91 crystallography revealed an expanded substrate binding site that binds the divalent cation as
92 complex with most of its hydration shell, which permits selection against the larger Ca^{2+}, which is
93 not a transported substrate.

94

95 **Results**

96 **Phylogenetic analysis of NRAMP transporters**

97 In light of the proposed altered substrate preference of certain prokaryotic SLC11 proteins, we
98 became interested in the phylogeny of the family. For that purpose, we have identified numerous
99 SLC11 homologues in BLAST searches of pro- and eukaryotic sequence databases using human
100 DMT1, the prokaryotic Mn^{2+} transporters EcoDMT and ScaDMT, the putative NRAMP-related
101 aluminium transporter (NRAT) from *Orzya sativa* and the proposed Mg^{2+} transporter CabNRMT
102 as queries. In this way sequences of 1,100 eukaryotic and 447 prokaryotic NRAMP proteins and
103 745 prokaryotic NRMTs were aligned and subjected to phylogenetic characterization. The
104 resulting phylogenetic tree displayed in Figure 1 shows a distributed organization with different
105 family members clustering into separated clades. Branches of this phylogenetic tree group proteins
106 from the animal kingdom including human DMT1 and NRAMP1, which both function as H^+
107 coupled Fe^{2+} transporters (Forbes and Gros, 2003; Gunshin et al., 1997), prokaryotic homologues
108 including proteins of known structure such as ScaDMT (Ehrnstorfer et al., 2014), EcoDMT
109 (Ehrnstorfer et al., 2017) and DraNRAMP (Bozzi et al., 2019b), whose primary function is H^+
110 coupled Mn^{2+} transport and plant proteins ascribed to be involved in the transport of various

111 transition metal ions such as the toxic metal Cd^{2+} (Huang et al., 2020a). Within the plant kingdom,
112 a small but separated branch encompasses putative Al^{3+} transporters classified as NRATs
113 (Chauhan et al., 2021; Xia et al., 2010). Finally, a large and distant clade of the family containing
114 homologues of the prototypic CabNRMT defines a group of transporters which, although clearly
115 being part of the family, appear to have evolved to serve a different purpose (Figure 1B) (Shin et
116 al., 2014). The proposed functional distinction between different clades is manifested in the
117 sequence of the substrate binding site that was identified in structural studies of prokaryotic SLC11
118 family members to coordinate divalent transition metals (Ehrnstorfer et al., 2014) (Figure 1A,
119 Figure 1—figure supplement 1). This site is defined by a signature containing a DxxN motif in the
120 unwound center of α-helix1 and an A/CxxM motif in the unwound center of α-helix 6. The
121 signature is fully conserved in Fe^{2+} transporters from animals, bacterial Mn^{2+} transporters and most
122 transporters of plant origin, which all exhibit a strong selectivity against alkaline earth metal ions
123 but poor discrimination between transition metal ions. Conversely, the motif is replaced by a
124 DxxN-AxxT motif in NRATs and a DxxG-TxxA/T motif in NRMTs thus indicating that latter
125 clades would exhibit a different substrate preference (Figure 1—figure supplement 1).

126

127 **Functional characterization of EcoDMT mutants**

128 To gain further insight into the presumed substrate preference, we investigated how mutations of
129 ion binding site residues would alter the selectivity of a classical NRAMP protein by characterizing
130 the functional properties of the bacterial Mn^{2+} transporter EcoDMT. To do so, we employed
131 previously established proteoliposome-based transport assays with appropriate fluorophores to
132 detect the uptake of specific ions into vesicles (Ehrnstorfer et al., 2017).

133 Classical NRAMP proteins efficiently transport divalent transition metal ions with low micromolar
134 affinity while discriminating against alkaline earth metal ions such as Ca^{2+} and Mg^{2+} (Ehrnstorfer
135 et al., 2017; Mackenzie et al., 2006). These functional properties are reflected in transport studies
136 of EcoDMT, which employ the fluorophore calcein as efficient reporter to monitor micromolar
137 concentrations of Mn^{2+} whereas it is not responsive to either Ca^{2+} or Mg^{2+} even at much higher
138 concentrations. In our experiments, we find a concentration-dependent quenching of the
139 fluorescence due to Mn^{2+} influx into the vesicles containing the trapped fluorophore (Figure 2A,
140 B), which is neither inhibited by the addition of Ca^{2+} nor Mg^{2+} to the outside solution (Figure 2C,
141 D). Latter would be expected if these ions would compete for the binding of Mn^{2+}. As suggested
142 from previous studies (Bozzi et al., 2016a; Ehrnstorfer et al., 2014), we expected a key role of the
143 methionine (Met 235) in the binding site of the protein as major determinant of this pronounced
144 selectivity. We thus initially investigated whether it was possible to alter the substrate preference
145 of EcoDMT by shortening the methionine side chain in the mutant EcoDMT M235A. This
146 construct was still capable of transporting Mn^{2+} with a threefold increase of its K_m (Figure 2A, B,
147 E, G), whereas now also Ca^{2+} became a permeable substrate as illustrated by the competition of
148 the ion with Mn^{2+} transport (Figure 2F, G) and the direct detection of Ca^{2+} transport using the
149 fluorophore Fura2 (Figure 2H). A similar result was previously obtained for the equivalent
150 mutation of the homologous DraNRAMP (Bozzi et al., 2016a). In contrast to Ca^{2+}, we were not
151 able to detect any interaction with Mg^{2+} (Figure 2I), indicating that the energetic requirements to
152 transport this smaller divalent cation are higher than for Ca^{2+}.

153 Finally, we attempted to confer Mg^{2+} transport properties to EcoDMT by creating the triple mutant
154 M235A/N54G/A232T, which converts its entire binding site to the residues found in prokaryotic
155 NRMTs. As for the mutant M235A, this construct folded into a stable protein that retained its

156 capability of Mn^{2+} transport while remaining unable to interact with Mg^{2+} (Figure 2J-L). In
157 summary, the mutation of the binding site residues of EcoDMT towards an NRMT was well
158 tolerated with the resulting constructs retaining their capability for Mn^{2+} transport. This suggests
159 that the structural and energetic requirements for interactions with this transition metal are lower
160 than for alkaline earth metals. We also confirmed the role of the binding site methionine as an
161 important determinant for the counterselection of Ca^{2+}, which due to its much higher concentration
162 would outcompete Mn^{2+} transport in a physiological environment. However, neither the
163 replacement of the methionine nor the conversion of the binding site to residues observed in
164 NRMTs was sufficient to facilitate Mg^{2+} transport, demonstrating that structural features beyond
165 the immediate binding site residues are required to transport this small divalent cation.
166 Consequently, we decided to turn our attention towards the characterization of prokaryotic NRMTs
167 to gain further insight into Mg^{2+} transport by SLC11 homologues.

168

169 **Functional characterization of EleNRMT**

170 Initially, our attempts towards the characterization of NRMTs were focused on the identification
171 of a suitable candidate for structural and functional studies. Towards this end we cloned and
172 investigated the expression properties of 82 representative homologues selected from the pool of
173 745 sequences of putative NRMTs identified in BLAST searches (Figure 1B). Within this subset,
174 we were able to single out a candidate from the bacterium *Eggerthella lenta* termed EleNRMT
175 with promising biochemical properties (Figure 3—figure supplement 1). After expression and
176 purification in the detergent n-dodecyl-beta-D-Maltoside (DDM), we found this protein to elute as
177 monodisperse peak from a size exclusion chromatography column. (Figure 3—figure supplement
178 2A). Although much better behaved than the other investigated homologues, EleNRMT was still

179 comparably instable in detergent solution and difficult to reconstitute into liposomes. We thus
180 attempted to improve its stability by consensus mutagenesis (Cirri et al., 2018) by converting 9
181 positions identified in sequence alignments to their most abundant residues in NRMTs to create
182 the construct EleNRMT^{ts} (Figure 3—figure supplement 1A). This approach improved the thermal
183 stability of the monomeric protein and the efficiency of reconstitution without affecting its
184 functional properties (Figure 3, Figure 3—figure supplement 2B-D). Due to the sensitivity of the
185 assay and the fact that binding site mutants of EcoDMT retained their ability to transport Mn^{2+},
186 we initially investigated transport properties of EleNRMT for this divalent transition metal ion and
187 found robust concentration-dependent activity that saturates with a K_m of around 120 µM for either
188 WT or the thermostabilized mutant (Figure 3A, B, D, E). For both constructs, we found Mg^{2+} to
189 inhibit Mn^{2+} transport in a concentration-dependent manner, thus indicating that Mg^{2+} would
190 compete with Mn^{2+} for its binding site (Figure 3C, F). We subsequently quantified binding of
191 either ion to detergent solubilized protein by isothermal titration calorimetry and found a K_d of
192 around 100 µM for Mn^{2+}, which corresponds well with the measured K_m of transport of the same
193 ion and a somewhat lower affinity of around 400 µM for Mg^{2+} (Figure 3G, H, Figure 3—figure
194 supplement 2E, F). Together, transport and binding experiments demonstrate the capability of
195 EleNRMT to interact with Mg^{2+} thus providing evidence that it might indeed catalyze Mg^{2+} uptake
196 into bacteria.

197 To further characterize Mg^{2+} transport by EleNRMT, we have quantified Mn^{2+} uptake into
198 proteoliposomes in presence of Mg^{2+} and found a strong interference (Figure 4A, B). By directly
199 assaying Mg^{2+} with the selective fluorophore Magnesium Green, we observed a concentration-
200 dependent increase of the transport rate (Figure 4C), with the lack of saturation at high substrate
201 concentrations reflecting the poor affinity of the dye for the ion. Since our experiments have

202 confirmed Mg^{2+} as substrate of EleNRMT, we wondered whether the protein would also transport
203 Ca^{2+} and thus investigated the inhibition of Mn^{2+} uptake by Ca^{2+} and the import of Ca^{2+} into
204 proteoliposomes monitored with the fluorophore Fura-2 (Figure 4D, E). However, in contrast to
205 Mg^{2+}, we did in no case find strong evidence for the recognition of this larger alkaline earth metal
206 ion, which has become a transported substrate for EcoDMT mutants lacking a conserved Met in
207 the binding site (Figure 2F-H). Latter finding is remarkable since the presumed metal ion binding
208 site only consists of hard ligands that would also coordinate Ca^{2+} and it thus emphasizes the
209 presence of distinct structural features of the pocket facilitating Mg^{2+} interactions (Figure 3—
210 figure supplement 1B).

211 After confirming the capability of EleNRMT to specifically transport Mn^{2+} and Mg^{2+}, we were
212 interested whether the uptake of metal ions would be coupled to H^+ as observed for previously
213 characterized transition metal ion transporters of the family. To this end we employed the
214 fluorophore ACMA to monitor pH changes that are induced by metal ion symport (Figure 4F-H).
215 Whereas such concentration-dependent changes are readily observed for EcoDMT (Figure 4H),
216 there was no acidification of proteoliposomes containing EleNRMT as a consequence of either
217 Mg^{2+} or Mn^{2+} uptake (Figure 4F, G), thus suggesting that metal ion transport by EleNRMT is not
218 coupled to H^+. Collectively our functional experiments confirm the role of EleNRMT to function
219 as uncoupled Mg^{2+} transporter. Due to the high sequence conservation in this subclade of the
220 SLC11 family, it is safe to assume that this property would likely also be shared by other NRMTs.

221

222 **Structural characterization of EleNRMT**

223 Following the characterization of the transport properties of EleNRMT, we became interested in
224 the molecular determinants underlying its distinct selectivity and thus engaged in structural studies
225 by X-ray crystallography and cryo-EM. Since the monomeric protein, with a molecular weight of
226 only 47 kDa and lacking pronounced domains extending from the membrane, is itself not a suitable
227 target for cryo-EM, we initially attempted structural studies by X-ray crystallography but were
228 unable to obtain crystals, despite extensive screening. To enlarge the size of the protein and
229 facilitate crystallization, we generated specific nanobodies by immunization of alpacas with
230 purified EleNRMT^{ts} followed by the assembly of a nanobody library from blood samples and
231 selection by phage display. These experiments allowed us to identify three distinct binders
232 recognizing the protein termed Nb1-3^{EleNRMT} (short Nb1-3) (Figure 4—figure supplement 1A).
233 Despite the increase of the hydrophilic surface, which was frequently found to facilitate
234 crystallization, all attempts to obtain crystals of EleNRMT^{ts} in complex with a single nanobody
235 were unsuccessful. Similarly, efforts towards the structure determination of the same complexes
236 by cryo-EM did not permit a reconstruction at high resolution. We thus attempted to further
237 increase the size of the complex and found that Nb1 and either one of the two closely related
238 nanobodies Nb2 or Nb3 were able to bind concomitantly to the protein to assemble into a ternary
239 complex (Figure 4—figure supplement 1B-D). This complex showed improved crystallization
240 properties and was of sufficient size to allow structure determination by single particle averaging.
241 The structure of the tripartite EleNRMT^{ts} nanobody complex was determined by cryo-EM in
242 absence of additional Mg^{2+} (EleNRMT^{ts}-Nb1,2) and in buffer containing 10 mM Mg^{2+}
243 (EleNRMT$^{ts}Mg^{2+}$-Nb1,2). Datasets collected from respective samples allowed the 3D-
244 reconstruction of a map at 3.5 Å for EleNRMT^{ts}-Nb1,2 and at 4.1 Å for EleNRMT$^{ts}Mg^{2+}$-Nb1,2
245 (Figure 5—figure supplements 1 and 2, Table 1). Both maps display equivalent conformations of

246 the complex and permitted its unambiguous interpretation by an atomic model defining the features
247 of an NRMT (Figure 5A, B, Figure 5—figure supplement 3). The structures show a protein
248 complex consisting of the transporter EleNRMT^{ts} and two nanobodies binding to non-overlapping
249 epitopes on the extracellular side (Figure 5A and B, Figure 5—figure supplement 4). This complex
250 structure was subsequently used as search model for molecular replacement for a dataset collected
251 from a crystal of the EleNRMT^{ts}-Nb1,2 complex grown in presence of 50 mM Mg^{2+} and extending
252 to 4.1 Å (Figure 5—figure supplement 5A, Table 2). In the X-ray structure, both copies of the
253 complex in the asymmetric unit closely resembled the cryo-EM model, thus providing an ideal
254 system to determine the location of bound ions by anomalous scattering experiments (Figure 5—
255 figure supplement 5A-C). Towards this end, we have soaked our crystals in solutions where Mg^{2+}
256 was replaced by Mn^{2+} in the expectation that latter would occupy the binding site as suggested
257 from functional experiments (Figure 3) and collected data at the anomalous absorption edge of the
258 transition metal ion. This data allowed the unambiguous localization of Mn^{2+} in the anomalous
259 difference density, which showed a single strong peak per complex located in the equivalent
260 position as previously identified for the binding site of ScaDMT (Ehrnstorfer et al., 2014) (Figure
261 5C, Figure 5—figure supplement 5B, C). In similar location, we find residual density in our cryo-
262 EM datasets thus suggesting that Mg^{2+} and Mn^{2+} would both occupy the same site of the transporter
263 (Figure 5—figure supplement 5D, E).

264

265 **EleNRMT structure and ion coordination**

266 The structure of EleNRMT^{ts} shows a transporter that displays the general organization of the
267 SLC11 family. It encompasses 11 membrane-spanning segments, with the first 10 segments
268 organized as two structurally related repeats of 5 α-helices that are inserted in the membrane with

269 opposite orientations (Figure 6A, Figure 3—figure supplement 1). The protein adopts an inward-
270 facing conformation that is illustrated in the comparison with the equivalent conformations of the
271 transporters ScaDMT and DraNRAMP, which both superimpose with RMSDs of 2.2 and 2.0 Å,
272 respectively (Figure 6B). This structure contains a large and continuous water-filled cavity that
273 extends from the cytoplasm and leads to a pocket located in the center of the protein at the unwound
274 parts of α-helices 1 and 6, which together form the ion binding site (Figures 5C and 6C). The
275 location of the bound ion is defined in the anomalous difference density of Mn^{2+} and its position
276 presumably also corresponds to the binding position of Mg^{2+} (Figure 5C, Figure 5—figure
277 supplement 5B-E). Although the bound ion is found at an equivalent position as in the transporter
278 ScaDMT, the binding pocket of EleNRMT is expanded as a consequence of the about 1.5 Å shift
279 in the location of backbone atoms and differences in the volume of interacting side chains (Figure
280 7A-C). In both, Mg^{2+} and Mn^{2+} transporters, an Asp on α-helix 1 and a main chain interaction at
281 the site of the unwound part of α-helix 6a remain a common feature of their binding sites, whereas
282 the replacement of an alanine (Ala 223) in ScaDMT by a threonine (Thr 224) in EleNRMT
283 introduces a side chain containing a hydroxyl group whose oxygen atom serves as additional ligand
284 for ion interactions (Figure 7B). Further changes of other residues of the binding site alter its shape
285 and volume. In ScaDMT, the bound ion is to a large extent excluded from the aqueous environment
286 and instead tightly surrounded by residues of the binding site, whereas in EleNRMT the
287 replacement of the asparagine side chain on α1 with a glycine and the methionine residue on α6 to
288 alanine in conjunction with differences in the main chain positions widen the cavity to leave
289 sufficient space for interacting water molecules (Figure 7A-C), suggesting that Mg^{2+} binds to the
290 transporter in a partly solvated state retaining much of its first hydration shell. Thus, the EleNRMT
291 structure implies that it is a combination of both, changes in the local environment conferred by

292 the chemical nature of side chains and more delocalized changes causing an expansion of the
293 binding site, which together are responsible for the altered selectivity.

294 Similar to the altered substrate preference, also the second functional hallmark of EleNRMT
295 concerning the absent coupling of metal ion transport to protons, is manifested in its structure
296 (Figure 7D, E). Proton coupling in classical NRAMP transporters was assigned to structural
297 features extending from the ion binding site (Bozzi et al., 2019a; Bozzi et al., 2020; Ehrnstorfer et
298 al., 2017; Mackenzie et al., 2006; Pujol-Gimenez et al., 2017). These include a conserved histidine
299 on α-helix 6b located two residues downstream of the binding site methionine and a continuous
300 path of acidic and basic residues on α-helices 3 and 9 surrounding a narrow aqueous cavity, which
301 together appear to constitute an intracellular H^+ release pathway. These residues are altered in
302 NRMTs where the histidine on α6 is replaced by a tryptophane, which cannot accept protons, and
303 where the polar pathway is filled by hydrophobic residues (Figure 7B, D. Figure 3—figure
304 supplement 1B).

305

306 **Functional properties of EleNRMT binding site mutants**

307 After identifying the structural determinants of ion interactions in NRMTs, we were interested in
308 the consequence of mutations of residues of the binding site on selectivity and thus investigated
309 the transport properties of mutants. Consistent with experiments on other family members, the
310 mutation of the aspartate in the binding site (Asp55), which is a universally conserved position in
311 all SLC11 proteins, strongly compromises transport (Figure 8A, B). Similarly, the mutation of Gln
312 379 on α10, a conserved position that was proposed to be involved in ion coordination in the
313 occluded state of DraNRAMP (Bozzi et al., 2019b), exerts a similarly strong effect (Figure 8A, C,

314 Figure 3–figure supplement 1B), thus suggesting that EleNRMT undergoes an equivalent
315 conformational change. In contrast, the mutation of Thr 224 to alanine, the amino acid found in
316 the equivalent position of NRAMP transporters, has smaller but still detectable impact on Mn^{2+}
317 transport, which is reflected in an at least two-fold increase of its K_m (Figures 8A, D, E). In contrast
318 to Mn^{2+}, this change has a much more pronounced effect on Mg^{2+} interactions, which is manifested
319 in the absence of appreciable inhibition of Mn^{2+} transport in presence of increasing Mg^{2+}
320 concentrations and the non-detectable Mg^{2+} transport when directly assaying this alkaline earth
321 metal ion (Figure 8F, G). Finally, by replacing Gly 88 to asparagine in the background of the
322 T224A mutant, we create an EleNRMT construct with a similar binding site signature as the
323 EcoDMT mutant M235A, which showed increased Ca^{2+} permeability. We thus investigated
324 whether an equivalent conversion would also change the properties of EleNRMT with respect to
325 its ability to transport Ca^{2+}, which is not a substrate of the WT protein (Figure 4D, E). In line with
326 the pronounced effect already observed for T224A (Figure 8D, E), we see a further reduction of
327 Mn^{2+} transport in the double mutant T224A/G88N (Figure 8H). In contrast to the compromised
328 Mn^{2+} transport properties, this double mutant shows detectable Ca^{2+} transport activity, thus
329 illustrating that the conversion has introduced structural determinants that facilitate Ca^{2+}
330 interactions and that change the properties of the binding site to more closely resemble NRAMP
331 proteins.

332

333 **Discussion**
334

335 In our study we have investigated the mechanistic basis of ion selectivity in the SLC11/NRAMP
336 family. Whereas the bulk of the family efficiently transports divalent transition metal ions such as
337 Fe^{2+} or Mn^{2+} from a high background of alkaline earth metal ions, there is an extended clade of

338 the family in prokaryotes that has evolved as transport systems of the divalent cation Mg^{2+} and
339 that were thus termed NRAMP related Mg^{2+} transporters (NRMTs) (Shin et al., 2014) (Figure 1).
340 These proteins are characterized by a distinct signature of residues constituting the ion binding
341 site, located in the center of the protein in the unwound parts of the pseudo-symmetry related
342 transmembrane helices α1 and α6 (Figs. 1, 7). We thus initially investigated whether we would be
343 able to confer the capability to transport Mg^{2+} to a transition metal ion transporter by mutation of
344 its ion binding site.

345 The most striking difference in the ion binding site of both clades of the NRAMP family concerns
346 the position of a conserved methionine that serves as a soft ligand for the interaction with transition
347 metal ions, which is replaced by an alanine in NRMTs (Figure 1). The mutation of this residue in
348 the classical NRAMP EcoDMT only moderately affected its capability to transport Mn^{2+} and
349 instead exerted its pronounced effect by converting Ca^{2+} into a transported substrate (Fig2 A-H).
350 This emphasizes the primary role of this residue to disfavor binding of this ubiquitous alkaline
351 earth metal ion, which was already proposed in a previous study (Bozzi et al., 2016a). Similarly,
352 an EcoDMT mutant where all three deviating residues of the binding site were mutated to their
353 correspondents found in NRMTs was still efficient in Mn^{2+} transport (Figure 2E), thus suggesting
354 that, among divalent cations, the transport of transition metal ions might not depend on stringent
355 structural prerequisites. In contrast to Ca^{2+}, neither of the mutants converted EcoDMT into a Mg^{2+}
356 transporter (Figure 2D, K), thus suggesting that the transport of latter might require specific
357 features to cope with the unique chemical properties of this ion. Among divalent cations of
358 biological relevance, Mg^{2+} is distinguished by its small ionic radius, which results in an unusually
359 strong interaction with the surrounding water molecules that would render its dehydration during
360 transport energetically costly (Persson, 2010). The first hydration shell of Mg^{2+}, which coordinates

361 the ion in an octahedral geometry (Figure 9A), was thus suggested to remain bound to the ion in
362 its initial encounter with the binding site and probably also during transport. A similar feature was
363 indeed observed in the structure of the unrelated bacterial Mg^{2+} transport proteins MgtE (Takeda
364 et al., 2014) and CorA (Guskov et al., 2012) whereas protein interactions in the membrane-inserted
365 domain of the transporter CorC are established with a fully dehydrated ion (Huang et al., 2021).

366 The distinct requirements for Mg^{2+} transport are reflected in the properties of EleNRMT
367 investigated in this study. Its capability to transport Mn^{2+} (Figure 3A-D, G) underlines the
368 described promiscuity of this ion in its interaction with proteins. In contrast, our studies have
369 shown transport of Mg^{2+} but not Ca^{2+} (Figs. 3E, F, H and 4A-E) thus illustrating that both ions rely
370 on distinct features of the protein which mediate their interaction. These are illustrated in the
371 structure of EleNRMT in an inward-facing conformation determined by cryo-EM (Figure 5 and
372 6). In this structure, a wide aqueous cavity leads to an ion binding site whose spacious volume
373 would preclude simultaneous interaction with a completely dehydrated ion (Figs 6C and 7B, C).
374 The larger size of the site is an immediate consequence of the decreased side chain-volume of the
375 surrounding residues concomitant with local differences in the backbone positions (Figure 7A, B),
376 which explains why it was impossible to convert EcoDMT into a Mg^{2+} transporter upon mutation
377 of respective residues (Figure 2D, I, K). The position of a Mn^{2+} ion bound to EleNRMT was
378 defined by its anomalous difference density in a crystal structure of the protein (Figure 5C). Since
379 Mn^{2+} shows a similar octahedral coordination as Mg^{2+}, although with weaker affinity to the
380 surrounding waters, we assume Mg^{2+} to bind in an equivalent manner, which is also reflected in
381 the presence of residual density in a dataset determined at high Mg^{2+} concentration by cryo-EM
382 (Figure 5-figure Supplement 5E). After placement of an octahedral Mg^{2+}-water complex, it is
383 apparent that only one of the solvent molecules would be replaced by a direct interaction with the

384 oxygen of the amide backbone group of Thr 224 whereas other interactions with the conserved
385 binding site would be mediated by coordinating waters (Figure 9B, C). The detailed structural
386 properties of this cavity are expected to change upon a transition from and inward-open into an
387 occluded intermediate conformation, which was observed in the corresponding structure of
388 DraNRAMP, where the access of the binding site to the cytoplasm is closed (Bozzi et al., 2019b).
389 However, in contrast to DraNRAMP, where the bound ion becomes tightly encircled by protein
390 residues, the distinct structural features of EleNRMT and the lower side chain volume of residues
391 of its binding site suggest that this cavity would be sufficiently big for Mg^{2+} to retain much of its
392 surrounding water during transport (Figure 9D-F) thus emphasizing that it is the larger hydrated
393 complex of Mg^{2+} rather than the naked ion that is relevant for transport.

394 A second pronounced feature that distinguishes EleNRMT and likely other NRMTs from classical
395 SLC11 proteins, concerns the absent coupling of metal ion transport to an energy source, which in
396 case of NRAMPS is conferred by the cotransport of protons (Ehrnstorfer et al., 2017; Gunshin et
397 al., 1997) (Figure 4F-H). This property is reflected in the location of ionizable residues that are
398 conserved within the proton- coupled part of the family and that are absent in EleNRMT (Figure
399 7E, F). It thus appears that in light of the high extracellular Mg^{2+} concentration and the inside
400 negative membrane potential such coupling may not be required for efficient uptake in the natural
401 habitat of the bacterium.

402 Collectively, the presented study has provided detailed mechanistic insight into the structural basis
403 of Mg^{2+} transport in homologues of the SLC11/NRAMP family and it has confirmed previous
404 results that have proposed this role based on biochemical considerations (Shin et al., 2014). Our
405 work also illustrates the promiscuity of transition metal ion transport, which contrasts the tight
406 requirements for the alkaline earth metal ions such as Ca^{2+} and Mg^{2+}, latter of which is transported

407 in a largely hydrated state. The observation that the previously investigated NRMT homologue did
408 not permit growth upon Mn^{2+} -limitation (Shin et al., 2014) could be a consequence of the lower
409 affinity to this ion, the competition with abundant Mg^{2+} and the absence of an energy source, which
410 might be mandatory for efficient accumulation of the scarce substrate. Our study illustrates the
411 specific requirements for the transport of Mg^{2+} which are not met by classical NRAMP
412 transporters. In respect, it appears unlikely that the human transporter SLC11A1, which resides in
413 the phagosomes of macrophages and is involved in the immune response against invading
414 microbes, would itself permit Mg^{2+} transport as suggested in a recent study (Cunrath and Bumann,
415 2019).

416

417 **Materials and Methods**

418 **Key resources table**

419

Reagent type	**Designation**	**Source or reference**	**Identifiers**	**Additional information**
Chemical compound, drug	1-palmitoyl-2-oleoyl-sn-glycero-3-phospho-(1'rac-glycerol) (18:1 06:0 POPG)	Avanti Polar Lipids	840457C	
Chemical compound, drug	E.coli polar extract	Avanti Polar Lipids	100600P	
Chemical compound, drug	1-palmitoyl-2-oleoyl-sn-glycero-3-phosphoethanolamine (18:1 06:0 POPE)	Avanti Polar Lipids	850757C	

Chemical compound, drug	Triton X-100	Sigma	Cat#T9284	
Chemical compound, drug	Lysozyme	Applichem	Cat#A3711	
Chemical compound, drug	Benzamidine	Sigma	B6506	
Chemical compound, drug	Chloroform	Fluka	25690	
Chemical compound, drug	DM	Anatrace	D322	
Chemical compound, drug	DDM	Anatrace	D310S	
Chemical compound, drug	Diethyl ether	Sigma	296082	
Chemical compound, drug	DNase I	AppliChem	A3778	
Chemical compound, drug	glycerol 99%	Sigma	G7757	
Chemical compound, drug	HCl	Merck Millipore	1.00319.1000	
Chemical compound, drug	HEPES	Sigma	H3375	
Chemical compound, drug	Imidazole	Roth	X998.4	
Chemical compound, drug	L-(+)-arabinose	Sigma	A3256	

Chemical compound, drug	Leupeptin	AppliChem	A2183	
Chemical compound, drug	Pepstatin	AppliChem	A2205	
Chemical compound, drug	Valinomycin	Thermofischer Scientific	V1644	
Chemical compound, drug	Calcimycin	Thermofischer Scientific	A1493	
Chemical compound, drug	Ionomycin	Thermofischer Scientific	I24222	
Chemical compound, drug	Fura2	Thermofischer Scientific	F1200	
Chemical compound, drug	Magnesium Green	Thermofischer Scientific	M3733	
Chemical compound, drug	ACMA	Thermofischer Scientific	A1324	
Chemical compound, drug	CCCP	Sigma	C2759	
Chemical compound, drug	Calcein	Thermofischer Scientific	C481	
Chemical compound, drug	Phosphate buffered saline	Sigma	D8537	
Chemical compound, drug	PEG400	Sigma	91893	
Chemical compound, drug	Manganese acetate	Sigma	330825	

Chemical compound, drug	Magnesium acetate	Fluka	63047	
Chemical compound, drug	Calcium Chloride	Sigma	223506	
Chemical compound, drug	Manganese Chloride	Fluka	31422	
Chemical compound, drug	Magnesium Chloride	Fluka	63065	
Chemical compound, drug	PMSF	Sigma	P7626	
Chemical compound, drug	Potassium chloride	Sigma	746346	
Chemical compound, drug	Sodium chloride	Sigma	71380	
Chemical compound, drug	Terrific broth	Sigma	T9179	
Commercial assay or kit	4–20% Mini-PROTEAN® TGX™ Precast Protein Gels, 15-well, 15 µl	BioRad Laboratories	4561096DC	
Commercial assay or kit	Amicon Ultra-4 Centrifugal Filters Ultracel 10K, 4 ml	Merck Millipore	UFC801096	
Commercial assay or kit	Amicon Ultra-4 Centrifugal Filters Ultracel 50K, 4 ml	Merck Millipore	UFC805096	
Commercial assay or kit	Amicon Ultra-4 Centrifugal Filters Ultracel 100K, 4 ml	Merck Millipore	UFC810024	

Commercial assay or kit	Biobeads SM-2 adsorbents	BioRad Laboratories	152-3920	
Commercial assay or kit	Avestin Extruder kit	Sigma	Cat#Z373 400	
Commercial assay or kit	400nm polycarbonate filters	Sigma	Cat#Z373 435	
Commercial assay or kit	96-well black walled microplates	Thermofischer Scientific	Cat#M330 89	
Commercial assay or kit	Ni-NTA resin	ABT Agarose Bead Technologies	6BCL-NTANi-X	
Commercial assay or kit	QuantiFoil R1.2/1.3 Au 200 mesh	Electron Microscopy Sciences	Q2100AR 1.3	
Commercial assay or kit	Superdex 200 10/300 GL	Cytiva	17517501	
Commercial assay or kit	Superdex 200 Increase 3.2/300	Cytiva	28990946	
Commercial assay or kit	Superdex 200 Increase 5/150 GL	Cytiva	28990945	
Commercial assay or kit	Superdex 75 10/300 GL	Cytiva	17517401	
Other	BioQuantum Energy Filter	Gatan	NA	
Other	HPL6	Maximator	NA	
Other	K3 Direct Detector	Gatan	NA	

Other	Titan Krios G3i	ThermoFisher Scientific	NA	
Other	Viber Fusion FX7 imaging system	Witec	NA	
Other	TECAN M1000 Infinite	TECAN	NA	
Other	Vitrobot Mark IV	ThermoFisher Scientific	NA	
Other	µDAWN MALS Detector	Wyatt Technology	NA	
recombinant DNA	gDNA Eggerthella lenta	DSMZ	2243	
recombinant DNA	gDNA Eremococcus coleocola	DSMZ	15696	
recombinant DNA	bacterial expression vector with C-terminal 3C cleavage site, GFP-tag and His-tag	Dutzler laboratory	NA	
recombinant DNA	bacterial expression vector with N-terminal His-tag and 3C cleavage site	Dutzler laboratory	NA	
recombinant DNA	bacterial expression vector with N terminal pelB sequence, His-tag, MBP, 3C cleavage site	Dutzler laboratory	NA	
recombinant protein	HRV 3C protease	Expressed (pET_3C) and purified in Dutzler laboratory	NA	
Software, algorithm	3DFSC	Tan et al., 2017	https://3dfsc.salk.edu/	

Software, algorithm	ASTRA7.2	Wyatt Technology	https://www.wyatt.com/products/software/astra.html	RRID: SCR_016255
Software, algorithm	Chimera v.1.15	Pettersen et al., 2004	https://www.cgl.ucsf.edu/chimera/	RRID: SCR_004097
Software, algorithm	ChimeraX v.1.1.1	Pettersen et al., 2021	https://www.rbvi.ucsf.edu/chimerax/	RRID: SCR_015872
Software, algorithm	Coot v.0.9.4	Emsley et al., 2010	https://www2.mrc-lmb.cam.ac.uk/personal/pemsley/coot/	RRID: SCR_014222
Software, algorithm	cryoSPARC v.3.0.1/v.3.2.0	Structura Biotechnology Inc.	https://cryosparc.com/	RRID: SCR_016501
Software, algorithm	DINO		http://www.dino3d.org	RRID: SCR_013497
Software, algorithm	EPU2.9	ThermoFisher Scientific	NA	
Software, algorithm	Phenix	Liebschner et al., 2019	https://www.phenix-online.org/	RRID: SCR_014224
Software, algorithm	RELION 3.0.7	Zivanov et al., 2018	https://www3.mrc-lmb.cam.a	RRID: SCR_016274

			c.uk/relion/	
Software, algorithm	WEBMAXC calculator	Bers et al., 2010	https://somapp.ucdmc.ucdavis.edu/pharmacology/bers/maxchelator/webmaxc/webmaxcS.htm	RRID: SCR_018807
Software, algorithm	JALVIEW	Waterhouse et al., 2009		
Software, algorithm	Muscle	Edgar, 2004		
Strain	E. coli MC1061	ThermoFisher Scientific	C66303	

420

421 **Phylogenetic Analysis of the SLC11 family**

422 The protein sequences of ScaDMT (UniprotKB A0A4U9TNH6), EcoDMT (UniprotKB
423 E4KPW4), hDMT1 (UniprotKB P49281), OsNRAT1 (Uniprot KB Q6ZG85), CabNRMT-c0685
424 (UniprotKB Q97L77) and CabNRMT-c3329 (UniprotKB Q97DZ1) were respectively used as
425 query sequences in BLASTp searches in diverse sequence databases. In that manner, 1100
426 eukaryotic and 447 prokaryotic standard SLC11 transporters and 745 prokaryotic NRMTs were
427 selected and aligned with CLC Main Workbench (Quiagen). The identity of the 745 prokaryotic

428 NRMTs was confirmed by individual inspection of the proposed ion binding site. A multiple
429 sequence alignment was used to generate a phylogenetic tree using the neighbor joining cluster
430 generation method. Protein distances were measured using a Jukes-Cantor model and a
431 Bootstrapping analysis was performed with 100 replicates.

432

433 **Expression and purification of EcoDMT**

434 EcoDMT and its mutants were expressed and purified as described previously (Ehrnstorfer et al.,
435 2017). Briefly, the vector EcoDMT-pBXC3GH (Invitrogen) was transformed into *E. coli* MC1061
436 cells and a preculture was grown in TB-Gly medium overnight using ampicillin (100 µg/ml) as a
437 selection marker for all expression cultures. The preculture was used at a 1:100 volume ratio for
438 inoculation of TB-Gly medium. Cells were grown at 37 °C to an OD_{600} of 0.7-0.9, after which the
439 temperature was reduced to 25 °C. Protein expression was induced by addition of arabinose to a
440 final concentration of 0.004% (w/v) for 12-14 h at 18 °C. Cells were harvested by centrifugation
441 for 20 min at 5,000 g, resuspended in buffer RES (200 mM NaCl, 50 mM KPi pH 7.5, 2 mM
442 $MgCl_2$, 40 µg/ml DNAseI, 10 µg/ml lysozyme, 1µM leupeptin, 1 µM pepstatin, 0.3 µM aprotinin,
443 1mM benzamidine, 1mM PMSF) and lysed using a high pressure cell lyser (Maximator HPL6).
444 After a low speed spin (10,000 g for 20 min), the supernatant was subjected to a second
445 centrifugation step (200,000 g for 45 min). The pelleted membrane was resuspended in buffer EXT
446 (200 mM NaCl, 50 mM KPi pH 7.5, 10% glycerol) at a concentration of 0.5 g of vesicles per ml
447 of buffer. The purification of EcoDMT and its mutants was carried out at 4°C. Isolated membrane
448 fractions were diluted 1:2 in buffer EXT supplemented with protease inhibitors (Roche cOmplete
449 EDTA-free) and 1% (w/v) n-decyl-β-D-maltopyranoside (DM, Anatrace). The extraction was
450 carried out under gentle agitation for 2 h at 4 °C. The lysate was cleared by centrifugation at

451 200,000 g for 30 min. The supernatant supplemented with 15 mM imidazole at pH 7.5 was
452 subsequently loaded onto NiNTA resin and incubated for at least 1 h under gentle agitation. The
453 resin was washed with 20 column volumes (CV) of buffer W (200 mM NaCl, 20 mM HEPES pH
454 7, 10% Glycerol, 50 mM imidazole pH 7.5, 0.25% (w/v) DM) and the protein was eluted with
455 buffer ELU (200 mM NaCl, 20 mM HEPES pH 7, 10% Glycerol, 200 mM imidazole pH 7.5,
456 0.25% (w/v) DM). Tag cleavage proceeded by addition of HRV 3C protease at a 3:1 molar ratio
457 and dialysis against buffer DIA (200 mM NaCl, 20 mM HEPES pH7, 10% Glycerol, 0.25% (w/v)
458 DM) for at least 2 h at 4 °C. After application to NiNTA resin to remove the tag, the sample was
459 concentrated by centrifugation using a 50 kDa molecular weight cutoff concentrator (Amicon) and
460 further purified by size exclusion chromatography using a Superdex S200 column (GE Healthcare)
461 pre-equilibrated with buffer SEC (200 mM NaCl, 20 mM HEPES pH 7, 0.25% (w/v) DM); The
462 peak fractions were pooled, concentrated, and used directly without freezing.
463
464 **Expression screening of NRMT homologues**
465 The DNA coding for NRMTs from 82 bacterial and archaeal strains were cloned from gDNA
466 (obtained from DSMZ) into pBXNHG3 or pBXC3H vectors (Invitrogen) using FX cloning
467 (Geertsma and Dutzler, 2011) providing a final construct where an NRMT contains a 10-His tag,
468 a GFP and a HRV 3C protease cleavage site fused to its N-terminus (pBXNHG3) or a HRV 3C
469 protease cleavage site and a 10-His tag fused to its C-terminus (pBXC3H). Both vectors contain
470 an arabinose promoter and an ampicillin resistance gene. Consequently, all cultures were
471 supplemented with 100 µg/ml ampicillin as selection marker. The vectors were transformed into
472 *E. coli* MC1061 cells and precultures were grown in Terrific Broth (TB) medium overnight. The
473 small-scale expression was performed in 24 well plates with gas permeable adhesive covers in TB

474 medium supplemented with 0.5% glycerol (TB-Gly). Each culture was inoculated at a 1:100
475 volume ratio. The cells were grown at 37 °C to an OD_{600} of 0.7-0.9, before the temperature was
476 reduced to 25 °C. The expression was induced by addition of arabinose to a final concentration of
477 0.001% (w/v) for 12-14 h at 18 °C. Cells were harvested by centrifugation for 20 min at 5,000 g,
478 resuspended in 400 µl of lysis buffer (200 mM NaCl, 50 mM KPi pH 7.5, 2 mM $MgCl_2$, 40 µg/mL
479 DNAseI, 1 µM leupeptin, 1 µM pepstatin, 0.3 µM aprotinin, 1 mM benzamidine, 1 mM PMSF).
480 Cells were lysed by disruption using sharp 500 µm glass beads. The supernatant was supplemented
481 with DDM at a final concentration of 1 % (w/v) and incubated for 1 h at 4 °C under gentle agitation.
482 The whole-cell extract was clarified by centrifugation at 200,000 g for 15 min and expressed
483 proteins not containing a fusion to a fluorescent protein were detected by Western blots. Constructs
484 fused to a fluorescent protein were detected by in-gel fluorescence imaging (Geertsma et al.,
485 2008a) and fluorescent size exclusion chromatography (FSEC) (Kawate and Gouaux, 2006) using
486 a Superdex S200 column connected to an Agilent HPLC system (GE Healthcare) (λ_{ex}=489 nm /
487 λ_{em}= 510 nm). The NRMT homologue (WP_114552427.1) from the prokaryote *Eggerthella lenta*
488 (DSM 2243, EleNRMT) was selected as the biochemically best-behaved homologue based on the
489 profile of the eluted peak. The stability of EleNRMT was further improved by mutagenesis. To
490 this end consensus amino acids were identified using JALVIEW (Waterhouse et al., 2009) from
491 aligned sequences of representative NRMT homologs, using Muscle (Edgar, 2004), and reported
492 criteria (Cirri et al., 2018).
493

494 **Expression and Purification of EleNRMT**

495 For large-scale overexpression, the DNA coding for the NRMT from the prokaryote *Eggerthella*
496 *lenta* (EleNRMT) was cloned into the pBXNH3 vector (Invitrogen) using the FX cloning

497 technique (Geertsma and Dutzler, 2011) providing a construct where *EleNRMT* contains a 10-His
498 tag and a HRV 3C protease cleavage site at its N-terminus. All mutants were generated using the
499 Quickchange site-direct mutagenesis method (Agilent). The vector was transformed into *E. coli*
500 MC1061 cells and a preculture was grown in TB-Gly medium overnight using ampicillin (100
501 μg/ml) as a selection marker for all expression cultures. The preculture was diluted at 1:100 volume
502 ratio into TB-Gly medium. The cells were grown at 37 °C to an OD_{600} of 0.7-0.9, before the
503 temperature was lowered to 25 °C. The expression was induced by addition of arabinose to a final
504 concentration of 0.0045% (w/v) for 12-14 h at 18 °C. Cells were harvested by centrifugation for
505 20 min at 5,000 g, resuspended in buffer RES and disrupted using a high-pressure cell lyser
506 (Maximator HPL6). After low spin centrifugation (10,000 g for 20min) to remove cell debris, the
507 supernatant was subjected to an ultracentrifugation step (200,000 g for 45 min) and the pelleted
508 membrane was resuspended in buffer EXT at a concentration of 0.5 g of vesicles per ml of buffer.
509 The purification of EleNRMT and its mutants was carried out at 4 °C. Suspended membrane
510 vesicles were diluted 1:2 in buffer EXT supplemented with protease inhibitors (Roche cOmplete
511 EDTA-free) and 1% (w/v) detergent, depending on the purpose of the experiments. DDM
512 (Anatrace) was used as detergent for proteoliposome-reconstitution and cryoEM sample
513 preparation and DM (Anatrace) for ITC and crystallization. The extraction was carried under
514 gentle agitation for 2 h at 4 °C. The lysate was cleared by centrifugation at 200,000 g for 30 min.
515 The supernatant supplemented with 15 mM of imidazole at pH 7.5 was loaded onto NiNTA resin
516 and incubated for at least 1 h under gentle agitation. During later stages of purification, the
517 detergent concentration was reduced to 0.04% (w/v) for DDM or 0.25% (w/v) for DM. The resin
518 was washed with 20 CV of buffer W and protein was eluted with buffer ELU, both containing the
519 respective detergent. The tag was cleaved by addition of HRV 3C protease at a 3:1 molar ratio and

520 dialyzed against buffer DIA containing the respective detergent for at least 2h at 4 °C. After
521 addition of NiNTA resin to remove the cleaved tag, the sample was concentrated by centrifugation
522 using a 50 kDa molecular weight cut-off concentrator (Amicon) and further purified by size
523 exclusion chromatography on a Superdex S200 column (GE Healthcare) pre-equilibrated with
524 buffer SEC containing the respective detergent. The peak fractions were pooled, concentrated, and
525 used immediately for further experiments.
526
527 **Reconstitution of EleNRMT and EcoDMT into proteoliposomes**
528 EleNRMT, EcoDMT and all of their mutants were reconstituted into detergent-destabilized
529 liposomes (Geertsma et al., 2008b). The lipid mixture made of POPE, POPG (Avanti Polar Lipids)
530 at a weight ratio of 3:1: was washed with diethylether and dried under a nitrogen stream followed
531 by exsiccation overnight. The dried lipids were resuspended in 100 mM KCl and 20 mM HEPES
532 at pH7. After 3 freeze-thaw cycles, the lipids were extruded through a 400 nm polycarbonate filter
533 (Avestin, LiposoFast-BAsic) and aliquoted into samples with a concentration of 45 mg/ml. The
534 extruded lipids were destabilized by adding Triton X-100 and the protein was reconstituted at a
535 lipid to protein ratio of 50. After several incubation rounds with biobeads SM-2 (Biorad), the
536 proteoliposomes were harvested the next day, resuspended in 100 mM KCl and 20 mM HEPES
537 pH7 and stored at -80 °C.
538
539 **Isothermal titration calorimetry**
540 A MicroCal ITC200 system (GE Healthcare) was used for Isothermal titration calorimetry
541 experiments. All titrations were performed at 6 °C in buffer SEC (200 mM NaCl, HEPES pH7,
542 0.25% DM). The syringe was filled with 3 mM $MnCl_2$ or $MgCl_2$ and the titration was initiated by

543 the sequential injection of 2 µl aliquots into the cell filled with EleNRMT or mutants at a
544 concentration of 70 µM. Data were analyzed with the Origin ITC analysis package and fitted
545 assuming a single binding site for metal ions and a stoichiometry of N = 1. Each experiment was
546 repeated twice from independent protein purifications with similar results. Experiments with
547 buffer not containing any protein were performed as controls.
548
549 **Fluorescence-based substrate transport assays**
550 The proteoliposomes were incubated with buffer IN (100 mM KCl, 20 mM HEPES pH 7,
551 containing either 250 µM Calcein (Invitrogen), 100 µM Fura-2 (ThermoFischer Scientific), or 400
552 µM MagGreen (ThermoFischer Scientific) depending on the assayed ion. After 3 cycles of freeze-
553 thawing, the liposomes were extruded through a 400 nm filter and the proteoliposomes were
554 centrifuged and washed 3 times with buffer IN not containing any fluorophores. The
555 proteoliposomes were subsequently diluted to 0.025 mg/ml in buffer OUT (100 mM NaCl, 20 mM
556 HEPES pH7) and aliquoted in 100 µl batches into a 96-well plate (ThermoFischer Scientific) and
557 the fluorescence was measured every 4 seconds using a Tecan Infinite M1000 fluorimeter. A
558 membrane potential was generated by addition of valinomycin to a final concentration of 100 nM.
559 After 20 cycles of incubation, the substrate was added at different concentrations. The transport
560 reaction was terminated by addition of calcimycin or ionomycin at a final concentration of 100
561 nM. The initial rate of transport was calculated by linear regression within the initial 100 seconds
562 of transport after addition of the substrate. The calculated values were fitted to a Michaelis-Menten
563 equation. Fura-2 was used to assay the transport of Ca^{2+}. For detection, the ratio between calcium
564 bound Fura-2 (λ_{ex}= 340 nm ; λ_{em}= 510 nm) and unbound Fura-2 (λ_{ex}= 380 nm ; λ_{em}= 510 nm) was
565 monitored during kinetic measurements. Calcein was used to assay the transport of Mn^{2+} (λ_{ex}=

566 492 nm ; λ_{em}= 518 nm) and Magnesium Green was to assay the transport of Mg^{2+} (λ_{ex}= 506 nm ;
567 λ_{em}= 531 nm).
568 For assaying coupled proton transport, the proteoliposomes were mixed with buffer 1 (100 mM
569 KCl, 5 mM HEPES pH 7, 50 µM ACMA). After clarification by sonication, the proteoliposomes
570 were diluted to a concentration of 0.15 mg/ml in buffer 2 (100 mM NaCl, 5 mM HEPES pH7) and
571 aliquoted into batches of 100 µl into a flat black 96-well plate (ThermoFischer Scientific). The
572 fluorescence was measured every 4 seconds using a fluorimeter Tecan Infinite M1000 (λ_{ex}= 412
573 nm; λ_{em}= 482 nm). The transport reaction was initiated after addition of the substrate and
574 valinomycin at a final concentration of 100 nM. The reaction was terminated by addition of CCCP
575 at 100 nM.
576
577 **Generation of nanobodies specific to EleNRMT**
578 EleNRMT specific nanobodies were generated using a method described previously (Pardon et al.,
579 2014). Briefly, an alpaca was immunized four times with 200 µg of detergent solubilized
580 $EleNRMT^{ts}$. Two days after the final injection, the peripheral blood lymphocytes were isolated
581 and the RNA total fraction was extracted and converted into cDNA by reverse transcription. The
582 nanobody library was amplified and cloned into the phage display pDX vector (Invitrogen). After
583 two rounds of phage display, ELISA assays were performed on the periplasmic extract of 198
584 individual clones. 3 nanobodies were identified. For all steps of phage display and ELISA, an
585 enzymatically biotinylated version of EleNRMT with an additional Avi tag on its N-terminus (Avi-
586 10His-3C) was used (Fairhead and Howarth, 2015) and bound to neutravidin coated plates. The
587 biotinylation was confirmed by total mass spectrometry analysis.
588

589 **Expression and purification of nanobodies and preparation of the EleNRMT^{ts}-Nb1,2**
590 **complex**

591 All nanobodies were cloned into the pBXNPHM3 vector (Invitrogen) using the FX cloning
592 technique. The expression construct contains the nanobody with a fusion of a pelB sequence, a 10-
593 His tag, a maltose-binding protein (MBP) and a HRV 3C protease site to its N-terminus. The vector
594 was transformed into *E. coli* MC1061 cells and a preculture was grown in TB-Gly medium
595 overnight using ampicillin (100 µg/ml) as a selection marker in all expression cultures. The
596 preculture was used for inoculation of TB-Gly medium at 1:100 volume ratio. Cells were grown
597 to an OD_{600} of 0.7-0.9 and the expression was induced by addition of arabinose to a final
598 concentration of 0.02% (w/v) for 4 h at 37 °C. Cells were harvested by centrifugation for 20 min
599 at 5,000 g, resuspended in buffer A (200 mM KCl, 50 mM KPi pH 7.5, 10% Glycerol, 15 mM
600 imidazole pH 7.5, 2 mM $MgCl_2$, 1µM leupeptin, 1 µM pepstatin, 0.3 µM aprotinin, 1mM
601 benzamidine, 1mM PMSF) and lysed using a high pressure cell lyser (Maximator HPL6). The
602 purification of all nanobodies was carried out at 4 °C. The lysate was cleared by centrifugation at
603 200,000 g for 30 min. The supernatant was loaded onto NiNTA resin and incubated for at least 1h
604 under gentle agitation. The resin was washed with 20 CV of buffer B (200 mM KCl, 20 mM
605 Tris.HCl pH8, 10% Glycerol, 50 mM imidazole, pH 7.5). The protein was eluted with buffer C
606 (200 mM KCl, 20 mM Tris.HCl pH 8, 10% Glycerol, 300 mM imidazole, pH 7.5). The tag was
607 cleaved by addition of HRV 3C protease at a 3:1 molar ratio and dialyzed against buffer D (200
608 mM KCl, 20 mM Tris.HCl pH8, 10% Glycerol) for at least 2 h at 4 °C. After application of NiNTA
609 resin to remove the tag, the sample was concentrated by centrifugation using a 10 kDa molecular
610 weight cut off concentrator (Amicon) and further purified by size exclusion chromatography using
611 a Superdex S200 column (GE Healthcare) pre-equilibrated with buffer E (200 mM KCl, 20 mM

612 Tris.HCl pH 8). The peak fractions were pooled, concentrated and flash-frozen and stored at -20
613 °C for subsequent experiments.
614 Following the purification of EleNRMT in DDM (for cryoEM data collection) or DM (for
615 crystallization) as described, the purified membrane protein and nanobodies Nb1 and Nb2 were
616 incubated at a 1:1.3:1.3 molar ratio for 30 min and the complex was further purified by size
617 exclusion chromatography on a Superdex S200 column (GE Healthcare), pre-equilibrated in the
618 same SEC buffer as used for EleNRMT purification. The sample was subsequently concentrated
619 to 3.5 mg/ml (for cryoEM) or 8-12 mg/ml (for crystallization).
620
621 **Cryo-EM sample preparation and data collection**
622 For sample preparation for cryo-EM, 2.5 µl of the complex were applied to glow-discharged holey
623 carbon grids (Quantifoil R1.2/1.3 Au 200 mesh). Samples were blotted for 2-4 s at 4 °C and 100%
624 humidity. The grids were frozen in liquid propane-ethane mix using a Vitrobot Mark IV (Thermo
625 Fisher Scientific). For the dataset in presence of Mg^{2+}, the sample was supplemented with 10 mM
626 $MgCl_2$ and incubated on ice for 20 min before grid preparation. All datasets were collected on a
627 300 kV Titan Krios (ThermoFischer Scientific) with a 100 µm objective aperture and using a post-
628 column BioQuantum energy filter with a 20 eV slit and a K3 direct electron detector in super-
629 resolution mode. All datasets were recorded automatically using EPU2.9 with a defocus ranging
630 from -1 to 2.4 µm, a magnification of 130,000x corresponding to a pixel size of 0.651 Å per pixel
631 (0.3255 Å in super resolution mode) and an exposure of 1.01s (36 frames). Three datasets were
632 collected for EleNRMT-Nb1,2 without $Mg^{2+}$with respective total doses of 69.725, 61 and 69.381
633 $e^-/Å^2$ and for EleNRMT-Nb1,2 with Mg^{2+} one dataset with a total dose of 69.554 $e^-/Å^2$
634

635

636 **Cryo-EM data processing**

637 Datasets were processed using Cryosparc v3.2.0 (Punjani et al., 2017) following the same
638 processing pipeline (Figure 5—figure supplements 1, 2). All movies were subjected to motion
639 correction using patch motion correction with a fourier crop factor of 2 (pixel size of 0.651 Å/pix).
640 After patch CTF estimation, high quality micrographs were identified based on relative ice
641 thickness, CTF resolution and total full frame motion and micrographs not meeting the specified
642 criteria were rejected. For the EleNRMT^{ts}-Nb1,2 complex, a partial dataset (981 micrographs) was
643 used to generate a low-resolution 3D *ab initio* model. For this purpose, particles were selected
644 using a blob picker with a minimum particle diameter of 160 Å and a minimum inter-particle
645 distance of 64 Å. The selected particles were extracted with a box size of 360 pixels and binned
646 4x (pixel size of 2.64 Å per pixel). These particles were initially used to generate 2D classes and
647 later for template-driven particle picking. After extraction and 2D classification, an initial 3D *ab*
648 *initio* model was generated in Cryosparc. This model was subsequently used to generate 2D
649 templates for particle picking on the remainder of the dataset.

650 The 2D classes generated from particles selected from the entire dataset were extracted using a
651 box size of 360 pix and down-sampled to 180 pixels (pixel size of 1.32 Å/pix). These particles
652 were used for generation of 4 *ab initio* classes. Promising *ab initio* models were selected based on
653 visual inspection and subjected to heterogenous refinement using one of the selected models as
654 'template' and an obviously bad model as decoy model. After several rounds of heterogenous
655 refinement, the selected particles and models were subjected to non-uniform refinement (input
656 model filtering to 8 Å) followed by local CTF refinement and another round of non-uniform
657 refinement. Finally, the maps were sharpened using the sharpening tool from the Cryosparc

658 package. The quality of the map was evaluated validated using 3DFSC (Tan et al., 2017) for FSC
659 validation and local resolution estimation.
660
661 **Cryo-EM model building and refinement**
662 Model building was performed in Coot (Emsley and Cowtan, 2004). Initially, the structure of
663 ScaDMT (PDB 5M94) was rigidly fitted into the densities and served as template for map
664 interpretation. The quality of the map allowed for the unambiguous assignment of residues 43-
665 438. The structure of Nb16 (PDB 5M94) was used to build Nb1 and Nb2. The model was
666 iteratively improved by real space refinement in PHENIX (Afonine et al., 2018) maintaining
667 secondary structure constrains throughout. Figures were generated using ChimeraX (Pettersen et
668 al., 2021) and Dino (http://www.dino3d.org). Surfaces were generated with MSMS (Sanner et al.,
669 1996).
670
671 **Crystallization and X-ray structure determination of the EleNRMT^{ts}-Nb1,2 complex**
672 The EleNRMT^{ts}-Nb1,2 complex was purified in DM as described before, supplemented with *E.*
673 *coli* polar lipids solubilized in DM to a final concentration of 100 µg/ml and used for the
674 preparation of vapor diffusion crystallization experiments in sitting drops by mixing 150 nl of the
675 concentrated protein with 150 nl of the mother liquor containing 50 mM MgAc, 50 mM HEPES
676 pH 7.2-7.6 and 25-30% PEG400. Crystals grew after 4 days and reached a maximum size of 0.2 x
677 0.3 x 0.3 mm after 12 days. The crystals were fished, cryoprotected by soaking into mother liquor
678 supplemented with PEG400 to a final concentration of 35% and flash frozen into liquid nitrogen.
679

680 All data sets were collected on frozen crystals on either the X06SA or the X06DA beamline at the
681 Swiss Light Source of the Paul Scherrer Institute (SLS, Villingen) on an EIGER 16M or PILATUS
682 2M-F detector (Dectris), respectively. Anomalous data were collected at the absorption edge of
683 manganese (1.896 Å). Integration and scaling was performed using XDS (Kabsch, 1993) and data
684 were further processed with CCP4 programs (CCP4, 1994). Phases were obtained by molecular
685 replacement in Phaser (McCoy et al., 2007). For the ternary complex EleNRMT- Nb1-Nb2, the
686 refined cryoEM structure was used as search model for the respective datasets. Structures were
687 refined in PHENIX (Liebschner et al., 2019) maintaining tight coordinate restraints and models
688 were inspected and modified in Coot (Emsley and Cowtan, 2004).
689

690 **Author Information**

691 The authors declare no competing financial interests. Correspondence and requests for materials
692 should be addressed to R.D. (dutzler@bioc.uzh.ch) and C.M. (c.manatschal@bioc.uzh.ch).
693

694 **Author Contributions**

695 K.R. cloned, expressed and purified proteins, performed transport assays and ITC experiments,
696 prepared samples for X-ray crystallography and cryo-EM. M.S.S. collected cryo-EM data. K. R.
697 processed cryo-EM data and built models. C.M. and K.R. collected and processed ITC and X-ray
698 data. K.R., C.M. and R.D. jointly planned experiments, analyzed data and wrote the manuscript.

699

700 **Data availability**

701 The cryo-EM density maps of the EleNRM-Nb complex in absence and presence of Mg^{2+} have
702 been deposited in the Electron Microscopy Data Bank under ID codes EMD-XXX and EMD-
703 YYY, respectively. The coordinates for the atomic model of the EleNRM-Nb complex in absence
704 of Mg^{2+} refined against the 3.4 Å cryo-EM density and the coordinates of the EleNRMT^{ts}-Nb1,2
705 complex in presence of Mg^{2+} refined against the 4.1 Å cryo-EM density have been deposited in
706 the Protein Data Bank under ID codes XXX and YYY. The coordinates and structure factors of
707 the EleNRMT^{ts}-Nb1,2 complexes in Mg^{2+} and Mn^{2+} have been deposited in the Protein Data Bank
708 with the accession codes XXX and YYY.

709

710 **Acknowledgements**

711 This research was supported by the Swiss National Science Foundation (SNF) through the National
712 Centre of Competence in Research TransCure. We thank Dr. Nicolas Reyes for his help with the
713 identification of positions for thermostabilization of EleNRMT and Dr. Marta Sawicka for input
714 in cryo-EM and help during initial sample characterization. Nanobodies were generated with the
715 help of the Nanobody Service Facility of UZH with the help of Dr. Sasia Stefanic. The assistance
716 of Yvonne Neldner during library generation is acknowledged. The cryo-electron microscope and
717 K3-camera were acquired with support of the Baugarten and Schwyzer-Winiker foundations and
718 a Requip grant of the Swiss National Science Foundation. We thank Simona Sorrentino and the
719 Center for Microscopy and Image Analysis (ZMB) of the University of Zurich for their support
720 and access to the electron microscope and Beat Blattmann of the Protein Crystallization Center of
721 the Department of Biochemistry for help with crystallization screening. X-ray data were collected
722 at the X06SA and X06DA Beamlines at the Swiss Light Source of the Paul Scherrer Institute. All
723 members of the Dutzler lab are acknowledged for help in various stages of the project.

724

725 **Competing financial interests**

726 The authors declare no competing financial interests.

727

728 **References**

729 Afonine, P.V., B.K. Poon, R.J. Read, O.V. Sobolev, T.C. Terwilliger, A. Urzhumtsev, and P.D.
730 Adams. 2018. Real-space refinement in PHENIX for cryo-EM and crystallography. *Acta*
731 *Crystallogr D Struct Biol*. 74:531-544.
732 Bozzi, A.T., L.B. Bane, W.A. Weihofen, A.L. McCabe, A. Singharoy, C.J. Chipot, K. Schulten,
733 and R. Gaudet. 2016a. Conserved methionine dictates substrate preference in Nramp-
734 family divalent metal transporters. *Proc Natl Acad Sci U S A*. 113:10310-10315.
735 Bozzi, A.T., L.B. Bane, W.A. Weihofen, A. Singharoy, E.R. Guillen, H.L. Ploegh, K. Schulten,
736 and R. Gaudet. 2016b. Crystal Structure and Conformational Change Mechanism of a
737 Bacterial Nramp-Family Divalent Metal Transporter. *Structure*. 24:2102-2114.
738 Bozzi, A.T., L.B. Bane, C.M. Zimanyi, and R. Gaudet. 2019a. Unique structural features in an
739 Nramp metal transporter impart substrate-specific proton cotransport and a kinetic bias to
740 favor import. *J Gen Physiol*. 151:1413-1429.
741 Bozzi, A.T., A.L. McCabe, B.C. Barnett, and R. Gaudet. 2020. Transmembrane helix 6b links
742 proton and metal release pathways and drives conformational change in an Nramp-family
743 transition metal transporter. *J Biol Chem*. 295:1212-1224.
744 Bozzi, A.T., C.M. Zimanyi, J.M. Nicoludis, B.K. Lee, C.H. Zhang, and R. Gaudet. 2019b.
745 Structures in multiple conformations reveal distinct transition metal and proton pathways
746 in an Nramp transporter. *Elife*. 8.
747 Carafoli, E., and J. Krebs. 2016. Why Calcium? How Calcium Became the Best Communicator. *J*
748 *Biol Chem*. 291:20849-20857.
749 CCP4. 1994. Collaborative Computational Project Nr. 4. The CCP4 Suite: Programs for X-ray
750 crystallography. *Acta Crystallogr. D*. 50:760-763.
751 Chaudhari, M.I., J.M. Vanegas, L.R. Pratt, A. Muralidharan, and S.B. Rempe. 2020. Hydration
752 Mimicry by Membrane Ion Channels. *Annu Rev Phys Chem*. 71:461-484.
753 Chauhan, D.K., V. Yadav, M. Vaculik, W. Gassmann, S. Pike, N. Arif, V.P. Singh, R. Deshmukh,
754 S. Sahi, and D.K. Tripathi. 2021. Aluminum toxicity and aluminum stress-induced
755 physiological tolerance responses in higher plants. *Crit Rev Biotechnol*. 41:715-730.
756 Cirri, E., S. Brier, R. Assal, J.C. Canul-Tec, J. Chamot-Rooke, and N. Reyes. 2018. Consensus
757 designs and thermal stability determinants of a human glutamate transporter. *Elife*. 7.
758 Courville, P., R. Chaloupka, and M.F. Cellier. 2006. Recent progress in structure-function analyses
759 of Nramp proton-dependent metal-ion transporters. *Biochem Cell Biol*. 84:960-978.
760 Cunrath, O., and D. Bumann. 2019. Host resistance factor SLC11A1 restricts Salmonella growth
761 through magnesium deprivation. *Science*. 366:995-999.

762 de Baaij, J.H., J.G. Hoenderop, and R.J. Bindels. 2015. Magnesium in man: implications for health
763 and disease. *Physiol Rev*. 95:1-46.
764 Edgar, R.C. 2004. MUSCLE: multiple sequence alignment with high accuracy and high
765 throughput. *Nucleic Acids Res*. 32:1792-1797.
766 Ehrnstorfer, I.A., E.R. Geertsma, E. Pardon, J. Steyaert, and R. Dutzler. 2014. Crystal structure of
767 a SLC11 (NRAMP) transporter reveals the basis for transition-metal ion transport. *Nat*
768 *Struct Mol Biol*. 21:990-996.
769 Ehrnstorfer, I.A., C. Manatschal, F.M. Arnold, J. Laederach, and R. Dutzler. 2017. Structural and
770 mechanistic basis of proton-coupled metal ion transport in the SLC11/NRAMP family. *Nat*
771 *Commun*. 8:14033.
772 Emsley, P., and K. Cowtan. 2004. Coot: model-building tools for molecular graphics. *Acta*
773 *crystallographica*. 60:2126-2132.
774 Fairhead, M., and M. Howarth. 2015. Site-specific biotinylation of purified proteins using BirA.
775 *Methods Mol Biol*. 1266:171-184.
776 Forbes, J.R., and P. Gros. 2003. Iron, manganese, and cobalt transport by Nramp1 (Slc11a1) and
777 Nramp2 (Slc11a2) expressed at the plasma membrane. *Blood*. 102:1884-1892.
778 Geertsma, E.R., and R. Dutzler. 2011. A versatile and efficient high-throughput cloning tool for
779 structural biology. *Biochemistry*. 50:3272-3278.
780 Geertsma, E.R., M. Groeneveld, D.J. Slotboom, and B. Poolman. 2008a. Quality control of
781 overexpressed membrane proteins. *Proc Natl Acad Sci U S A*. 105:5722-5727.
782 Geertsma, E.R., N.A. Nik Mahmood, G.K. Schuurman-Wolters, and B. Poolman. 2008b.
783 Membrane reconstitution of ABC transporters and assays of translocator function. *Nat*
784 *Protoc*. 3:256-266.
785 Gunshin, H., B. Mackenzie, U.V. Berger, Y. Gunshin, M.F. Romero, W.F. Boron, S. Nussberger,
786 J.L. Gollan, and M.A. Hediger. 1997. Cloning and characterization of a mammalian proton-
787 coupled metal-ion transporter. *Nature*. 388:482-488.
788 Guskov, A., N. Nordin, A. Reynaud, H. Engman, A.K. Lundback, A.J. Jong, T. Cornvik, T. Phua,
789 and S. Eshaghi. 2012. Structural insights into the mechanisms of Mg2+ uptake, transport,
790 and gating by CorA. *Proc Natl Acad Sci U S A*. 109:18459-18464.
791 Huang, X., S. Duan, Q. Wu, M. Yu, and S. Shabala. 2020a. Reducing Cadmium Accumulation in
792 Plants: Structure-Function Relations and Tissue-Specific Operation of Transporters in the
793 Spotlight. *Plants (Basel)*. 9.
794 Huang, Y., R. Fliegert, A.H. Guse, W. Lu, and J. Du. 2020b. A structural overview of the ion
795 channels of the TRPM family. *Cell Calcium*. 85:102111.
796 Huang, Y., F. Jin, Y. Funato, Z. Xu, W. Zhu, J. Wang, M. Sun, Y. Zhao, Y. Yu, H. Miki, and M.
797 Hattori. 2021. Structural basis for the Mg(2+) recognition and regulation of the CorC
798 Mg(2+) transporter. *Sci Adv*. 7.
799 Kabsch, W. 1993. Automatic Processing of Rotation Diffraction Data from Crystals of Initially
800 Unknown Symmetry and Cell Constants. *J. Appl. Cryst.* 26:795-800.
801 Kawate, T., and E. Gouaux. 2006. Fluorescence-detection size-exclusion chromatography for
802 precrystallization screening of integral membrane proteins. *Structure*. 14:673-681.
803 Liebschner, D., P.V. Afonine, M.L. Baker, G. Bunkoczi, V.B. Chen, T.I. Croll, B. Hintze, L.W.
804 Hung, S. Jain, A.J. McCoy, N.W. Moriarty, R.D. Oeffner, B.K. Poon, M.G. Prisant, R.J.
805 Read, J.S. Richardson, D.C. Richardson, M.D. Sammito, O.V. Sobolev, D.H. Stockwell,
806 T.C. Terwilliger, A.G. Urzhumtsev, L.L. Videau, C.J. Williams, and P.D. Adams. 2019.

807 Macromolecular structure determination using X-rays, neutrons and electrons: recent
808 developments in Phenix. *Acta Crystallogr D Struct Biol*. 75:861-877.
809 Lunin, V.V., E. Dobrovetsky, G. Khutoreskaya, R. Zhang, A. Joachimiak, D.A. Doyle, A.
810 Bochkarev, M.E. Maguire, A.M. Edwards, and C.M. Koth. 2006. Crystal structure of the
811 CorA Mg2+ transporter. *Nature*. 440:833-837.
812 Mackenzie, B., M.L. Ujwal, M.H. Chang, M.F. Romero, and M.A. Hediger. 2006. Divalent metal-
813 ion transporter DMT1 mediates both H+ -coupled Fe2+ transport and uncoupled fluxes.
814 *Pflugers Arch*. 451:544-558.
815 Maguire, M.E. 1992. MgtA and MgtB: prokaryotic P-type ATPases that mediate Mg2+ influx. *J*
816 *Bioenerg Biomembr*. 24:319-328.
817 Maguire, M.E., and J.A. Cowan. 2002. Magnesium chemistry and biochemistry. *Biometals*.
818 15:203-210.
819 Makui, H., E. Roig, S.T. Cole, J.D. Helmann, P. Gros, and M.F. Cellier. 2000. Identification of
820 the Escherichia coli K-12 Nramp orthologue (MntH) as a selective divalent metal ion
821 transporter. *Mol Microbiol*. 35:1065-1078.
822 McCoy, A.J., R.W. Grosse-Kunstleve, P.D. Adams, M.D. Winn, L.C. Storoni, and R.J. Read.
823 2007. Phaser crystallographic software. *Journal of applied crystallography*. 40:658-674.
824 Montalbetti, N., A. Simonin, G. Kovacs, and M.A. Hediger. 2013. Mammalian iron transporters:
825 families SLC11 and SLC40. *Mol Aspects Med*. 34:270-287.
826 Nevo, Y., and N. Nelson. 2006. The NRAMP family of metal-ion transporters. *Biochim Biophys*
827 *Acta*. 1763:609-620.
828 Pardon, E., T. Laeremans, S. Triest, S.G. Rasmussen, A. Wohlkonig, A. Ruf, S. Muyldermans,
829 W.G. Hol, B.K. Kobilka, and J. Steyaert. 2014. A general protocol for the generation of
830 Nanobodies for structural biology. *Nat Protoc*. 9:674-693.
831 Payandeh, J., R. Pfoh, and E.F. Pai. 2013. The structure and regulation of magnesium selective ion
832 channels. *Biochim Biophys Acta*. 1828:2778-2792.
833 Persson, I. 2010. Hydrated metal ions in aqueous solution: How regular are their structures? *Pure*
834 *and Applied Chemistry*. 82:1901-1917.
835 Pettersen, E.F., T.D. Goddard, C.C. Huang, E.C. Meng, G.S. Couch, T.I. Croll, J.H. Morris, and
836 T.E. Ferrin. 2021. UCSF ChimeraX: Structure visualization for researchers, educators, and
837 developers. *Protein Sci*. 30:70-82.
838 Pujol-Gimenez, J., M.A. Hediger, and G. Gyimesi. 2017. A novel proton transfer mechanism in
839 the SLC11 family of divalent metal ion transporters. *Sci Rep*. 7:6194.
840 Punjani, A., J.L. Rubinstein, D.J. Fleet, and M.A. Brubaker. 2017. cryoSPARC: algorithms for
841 rapid unsupervised cryo-EM structure determination. *Nature Methods*. 14:290-296.
842 Sanner, M.F., A.J. Olson, and J.C. Spehner. 1996. Reduced surface: an efficient way to compute
843 molecular surfaces. *Biopolymers*. 38:305-320.
844 Schaffers, O.J.M., J.G.J. Hoenderop, R.J.M. Bindels, and J.H.F. de Baaij. 2018. The rise and fall
845 of novel renal magnesium transporters. *Am J Physiol Renal Physiol*. 314:F1027-F1033.
846 Schweigel-Rontgen, M., and M. Kolisek. 2014. SLC41 transporters--molecular identification and
847 functional role. *Curr Top Membr*. 73:383-410.
848 Shin, J.H., C.A. Wakeman, J.R. Goodson, D.A. Rodionov, B.G. Freedman, R.S. Senger, and W.C.
849 Winkler. 2014. Transport of magnesium by a bacterial Nramp-related gene. *PLoS Genet*.
850 10:e1004429.

851 Takeda, H., M. Hattori, T. Nishizawa, K. Yamashita, S.T. Shah, M. Caffrey, A.D. Maturana, R.
852 Ishitani, and O. Nureki. 2014. Structural basis for ion selectivity revealed by high-
853 resolution crystal structure of Mg2+ channel MgtE. *Nat Commun*. 5:5374.
854 Tan, Y.Z., P.R. Baldwin, J.H. Davis, J.R. Williamson, C.S. Potter, B. Carragher, and D. Lyumkis.
855 2017. Addressing preferred specimen orientation in single-particle cryo-EM through
856 tilting. *Nat Methods*. 14:793-796.
857 Tanaka, Y., M. Hattori, S. Fukai, R. Ishitania, and O. Nureki. 2007. Crystallization and preliminary
858 X-ray diffraction analysis of the cytosolic domain of the Mg2+ transporter MgtE. *Acta*
859 *Crystallogr Sect F Struct Biol Cryst Commun*. 63:678-681.
860 Waterhouse, A.M., J.B. Procter, D.M. Martin, M. Clamp, and G.J. Barton. 2009. Jalview Version
861 2--a multiple sequence alignment editor and analysis workbench. *Bioinformatics*. 25:1189-
862 1191.
863 Xia, J., N. Yamaji, T. Kasai, and J.F. Ma. 2010. Plasma membrane-localized transporter for
864 aluminum in rice. *Proc Natl Acad Sci U S A*. 107:18381-18385.
865 Yamashita, A., S.K. Singh, T. Kawate, Y. Jin, and E. Gouaux. 2005. Crystal structure of a bacterial
866 homologue of Na+/Cl--dependent neurotransmitter transporters. *Nature*. 437:215-223.
867

868

869 **Figures**

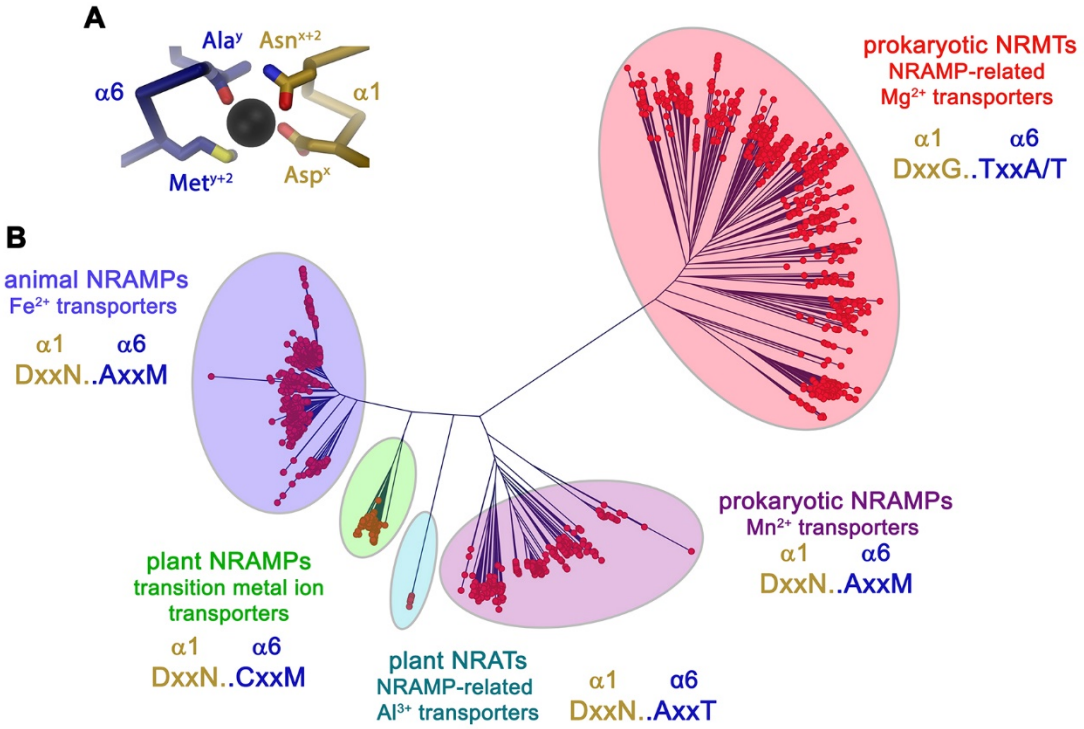

870

871 **Figure 1.** Phylogenetic analysis of the SLC11/NRAMP family. (**A**) Model of the consensus ion
872 binding site of NRAMP transporters as obtained from the X-ray structure of ScaDMT (PDBID
873 5M95) in complex with Mn^{2+}. Regions of α1 and α6 are shown as Cα-trace, selected residues
874 coordinating the ion as sticks. (**B**) Phylogenetic tree of SLC11 residues with different clades of the
875 family highlighted. The consensus sequence of the respective ion binding site of each clade is
876 shown.

877

878 The following figure supplements are available for figure 1:

879 **Figure supplement 1.** Sequence alignment of selected protein regions of SLC11 family members.

```
                    1a                  1b                  6a                  6b
prokaryotic
NRAMPs
prNRAMP1    PGLLVSVGYMDPGNWATAIEAGSRFG  YLAIGILGATVMPHNLYLHSSVV
prNRAMP2    PGLLVAVGYMDPGNWITSMQGGAQYG  YIALGIIGATIMPHNLYLHSSIV
prNRAMP3    PGALVAVGYMDPGNWSTSITGGQNFQ  SASLGIIGATIMPLNLFLHSAIS
prNRAMP4    PAFVAAIAYVDPGNVAANVSSGAQFG  LLAAAIMGATVMPHAVYLHSGLA
prNRAMP5    PAFIAAIAYIDPGNFATNISAGSKYG  LLAAAIMGATVMPHAVYLHSGLA
prNRAMP6    PAVIASIAYMDPGNFATNIEGGARYG  YLAVGIIGATVMPHVIYLHSALT
prNRAMP7    PAFIAAIGYIDPGNFATNIQAGASFG  FLAAGVLGATIMPHVIYLHSSLT
prNRAMP8    PAFIAAIGYIDPGNFATNIQAGASFG  FLAAGVLGATIMPHVIYLHSSLT

animal
NRAMPs
anNRAMP1    PGFLMSIAYLDPGNIESDLQSGAVAG  EQAVGIVGAVIMPHNMYLHSALV
anNRAMP2    PGFLMSIAYLDPGNIESDLQSGAVAG  EQAVGIVGAVIMPHNMYLHSALV
anNRAMP3    PGFLMSIAYLDPGNIESDLQSGAVAG  EQAVGIVGAVIMPHNMYLHSALV
anNRAMP4    PGFLMSIAYLDPGNIESDLQSGAVAG  EQAVGIVGAVIMPHNMYLHSALV
anNRAMP5    PGFLMSIAYLDPGNIESDLQSGAVAG  EQAVGIVGAVIMPHNMYLHSALV
anNRAMP6    PGFLMSIAYLDPGNIESDLQSGAVAG  EQAVGIVGAVIMPHNMYLHSALV
anNRAMP7    PGFLMSIAYLDPGNIESDLQSGAVAG  EQAVGIVGAVIMPHNMYLHSALV
anNRAMP8    PGFLMSIAYLDPGNIESDLQSGAVAG  EQAVGIVGAVIMPHNMYLHSALV
anNRAMP9    PGFLMSIAYLDPGNIESDLQSGAVAG  EQAVGIVGAVIMPHNMYLHSALV
anNRAMP10   PGFLMSIAYLDPGNIESDLQSGAVAG  EQAVGIVGAVIMPHNMYLHSALV

plant
NRAMPs
plNRAMP1    PGFLMSIAFLDPGNLEGDLQAGAIAG  QQAVGIVGCIIMPHNVFLHSALV
plNRAMP2    PGFLMSIAFLDPGNLEGDLQAGAIAG  RQAVGVVGCVIMPHNVYLHSALV
plNRAMP3    PGFLMSIAFLDPGNLEGDLQAGAIAG  QQAVGVVGCIIMPHNVFLHSALV
plNRAMP4    PGFLMSIAFLDPGNLEGDLQSGAIAG  QQAVGVVGCVIMPHNVYLHSALV
plNRAMP5    PGFLMSIAFLDPGNLEGDLQSGAIAG  QQAVGVVGCIIMPHNVFLHSALV
plNRAMP6    PGFLMSIAFLDPGNLEGDLQSGAIAG  QQAVGVVGCIIMPHNVFLHSALV
plNRAMP7    PGFLMSIAFLDPGNLEGDLQSGAIAG  QQAVGVVGCIIMPHNVFLHSALV
plNRAMP8    PGFLMSIAFLDPGNLEGDLQAGAIAG  QQAVGVVGCLIMPHNVFLHSALV
plNRAMP9    PGFLMSIAFLDPGNLEGDLQAGAIAG  QQAVGVVGCLIMPHNVFLHSALV
plNRAMP10   PGFLMSIAFLDPGNLEGDLQAGAIAG  QQAVGVVGCLIMPHNVFLHSALV

plant
NRATs
plNRAT1     PGALVAIGFLDPSNIETDMQAGAEFK  TNAIALFGSIITPYNLFLHSALV
plNRAT2     PGALVAIGFLDPSNLETDMQAGADFK  ANAIALFGAIITPYNLFLHSALV
plNRAT3     PGALVAIGFLDPSNLETDMQAGADFK  ANAIALFGAIITPYNLFLHSALV
plNRAT4     PGALVAIGFLDPSNLETDMQAGADFK  ANAIALFGAIITPYNLFLHSALV
plNRAT5     PGALVAIGFLDPSNLETDMQAGADFK  ANAIALFGAIITPYNLFLHSALV
plNRAT6     PGALVAIGFLDPSNMETDMQAGADFK  ANAIALFGAIITPYNLFLHSALV
plNRAT7     PGALVAIGFLDPSNLETDMQAGADFK  ANAIALFGAIITPYNLFLHSALV

prokaryotic
NRMTs
prNRMT1     PGIVTAMAGNDAGGISTYSTVGAKFG  SLVIAMIGTTIAPWMMFFNQSNV
prNRMT2     PGIIAASAGNDAGGITTYAMVGAELQ  TLFVGTVGTTIAPWMQFYLQSSI
prNRMT3     PGLVTATADNDASGIATYAMVGAMFG  LIFIAMIGTTITPWMQFYLQSSV
prNRMT4     PGLITVNAGNDAGGIATYATVGASYG  LTLIGMIGTTITPYMQFYLQSSV
prNRMT5     PGVITANAGNDAGGIATFASVGAEHG  FTLVAVIGTTISPYMQVFIQSSV
prNRMT6     PGFITAVVDNDSGGIFTYSAAGARFG  YMLIGMVGTTIAPWMQFYLQAAV
prNRMT7     PGIITANVDNDAGGITTYSITGATTG  SILIGFIGTTITPWMQFYIQSST
prNRMT8     PGIITANVDNDAGGITTYSLAAANYG  MTLIGIVGTTIAPWMQFYQQSAV
prNRMT9     PGIITSNVDNDAGGITTYSLAGAEYG  TMAIGLVGTTIAPWMQFYLQSSV
prNRMT10    PGIITANVDNDAGGITTYSVAGAQFG  MMIIGVVGTTIAPWMQFYLQSAV
prNRMT11    PGIITASVDNDAGGITTYSLAGARFG  LMLIGLVGTTIAPWMQFYIQSAI
```

880

881 **Figure 1—figure supplement 1.** Sequence alignment of selected protein regions of SLC11 family
882 members. Residues constituting the ion binding site are highlighted in green. Secondary structure
883 elements are indicated on the top. Prokaryotic NRAMPSs (prNRAMP): 1 *D. radiodurans*
884 (Uniprot: Q9RTP8), 2 *S. capitis* (Uniprot: A0A4U9TNH6), 3 *E. coelocola* (Uniprot: E4KPW4), 4
885 *E. coli* (UniProt: sp|*P0A769*|MNTH_ECOLI), 5 *M. tuberculosis* (UniProt:
886 sp|P9WIZ5|MNTH_MYCTU), 6 *B. subtilis* (UniProt: sp|P96593|MNTH_BACSU), 7 *S.*
887 *typhimurium* (Uniprot: sp|Q9RPF4|MNTH_SALTY), 8 *P. aeruginosa* (Uniprot:
888 sp|Q9RPF3|MNTH1_PSEAE).
889 Animal NRAMPs (anNRAMP): 1 *H. sapiens* NRAMP2 (NCBI: NP_001366375.1), 2 *P. paniscus*
890 NRAMP2 (NCBI: XP_008949491.1), 3 *C. sabaeus* NRAMP2 (NCBI: XP_037853046.1), 4 *R.*
891 *roxellana* NRAMP2 (NCBI: XP_010383634.1), 5 *M. mulatta* NRAMP2 (NCBI: EHH20731.1), 6
892 *E. caballus* NRAMP2 (NCBI: XP_023499318.1), 7 *C. canadensis* NRAMP2 (NCBI:
893 XP_020035491.1), 8 *H. hyaena* NRAMP2 (NCBI: XP_039097283.1), 9 *C. ferus* NRAMP2
894 (NCBI: XP_032348726.1), 10 *B. indicus* NRAMP2 (NCBI: XP_019816126.1).
895 Plant NRAMPs (plNRAMP): 1 *P. vulgaris* (NCBI: XP_007155869.1), 2 *T. subterraneum* (NCBI:
896 GAU12542.1), 3 *G. max* (NCBI: NP_001344702.1), 4 *C. arietinum* (NCBI: XP_004511877.1), 5
897 *D. chrysotoxum* (NCBI: KAH0462125), 6 *T. cacao* (NCBI: XP_007047433.1), 7 *V. unguiculata*
898 (NCBI: XP_027914252.1), 8 *G. soja* (NCBI: KAG4933418.1), 9 *M. truncatula* (NCBI:
899 XP_003611648.1), 10 *A. annua* (NCBI: PWA53748.1).
900 Plant NRATs (plNRAT): 1 *O. sativa* (NCBI: XP_015625418.1), 2 *D. oligosanthes* (NCBI:
901 OEL35611.1), 3 *S. italica* (NCBI: XP_004952002.1), 4 *S. bicolor* (NCBI: XP_002451480.2), 5 *P.*
902 *miliaceum* (NCBI: RLM80353.1), 6 *P. virgatum* (NCBI: XP_039819678.1), 7 *Z. mays* (NCBI:
903 PWZ19830.1).

904 Prokaryotic NRMTs (prNRMT): 1 *P. propionicus* (NCBI: WP_011735082.1), 2 *M. australiensis*
905 (NCBI: WP_013780282.1), 3 *C. saccharolyticus* (NCBI: WP_011916762.1), 4 *A. bacterium*
906 (NCBI: PYS45348.1), 5 *G. bemidjiensis* (NCBI: WP_012531668.1), 6 *T. narugense* (NCBI:
907 PMP85905.1), 7 *C. acetobutylicum* (NCBI: WP_034583260.1), 8 *M. paludicola* (NCBI:
908 BAI61876.1), *9 S. aciditrophicus* (NCBI: WP_011418107.1), 10 *S. usitatus* (NCBI:
909 WP_011688372.1), 11 *E. laentae* (NCBI: WP_009305646.1).

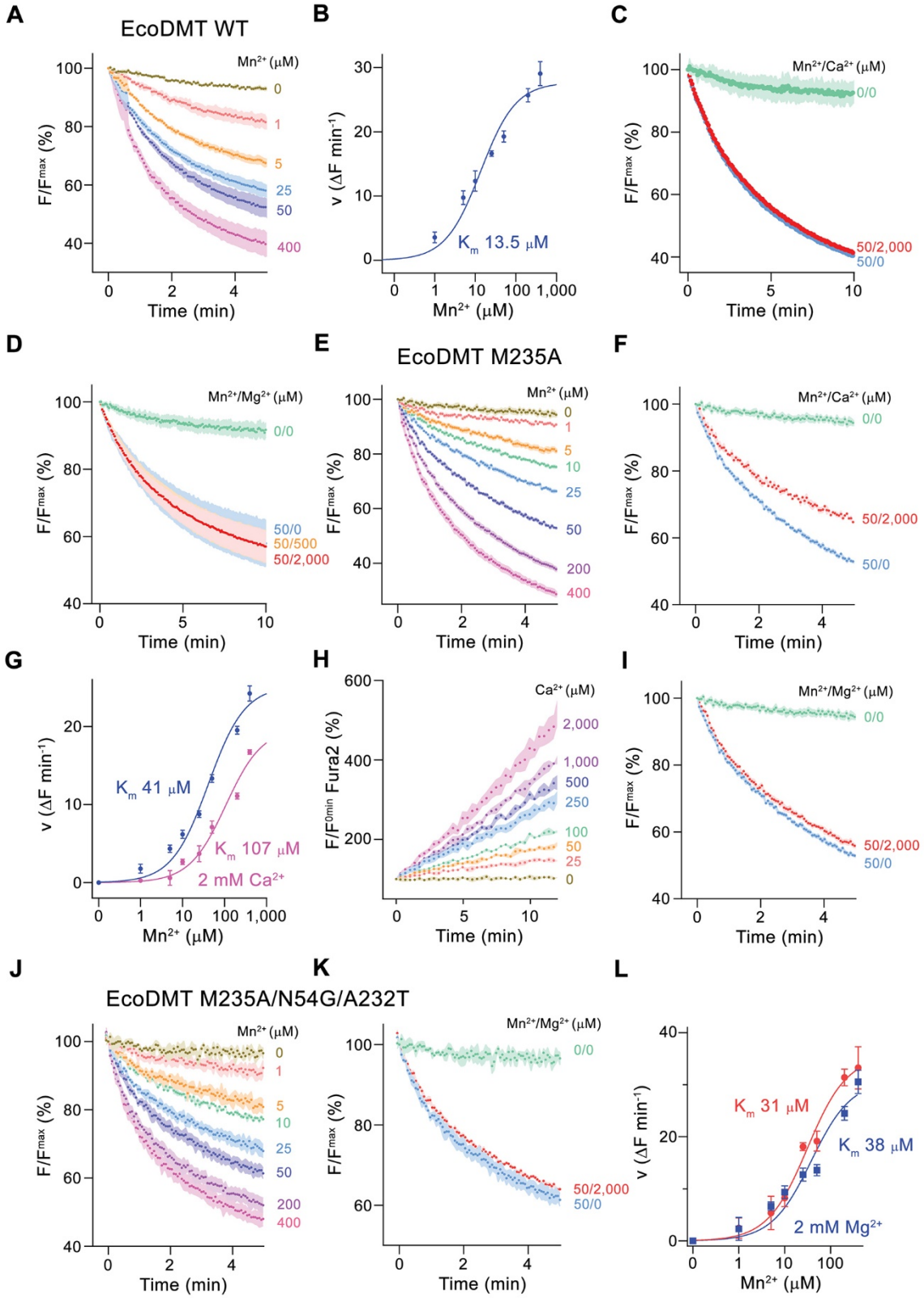
A
EcoDMT WT
Mn2+ (μM)
0
1
5
25
50
400
F/Fmax (%)
Time (min)
B
v (ΔF min-1)
Km 13.5 μM
Mn2+ (μM)
C
Mn2+/Ca2+ (μM)
0/0
50/2,000
50/0
D
Mn2+/Mg2+ (μM)
0/0
50/0
50/500
50/2,000
E
EcoDMT M235A
F
G
Km 41 μM
Km 107 μM
2 mM Ca2+
H
F/F0min Fura2 (%)
Ca2+ (μM)
2,000
1,000
500
250
100
50
25
0
I
J
EcoDMT M235A/N54G/A232T
K
L
Km 31 μM
Km 38 μM
2 mM Mg2+

910

911 **Figure 2.** Functional characterization of EcoDMT mutants. (**A**) EcoDMT mediated Mn^{2+} transport
912 into proteoliposomes. Data display mean of 3 experiments from 3 independent reconstitutions. (**B**)
913 Mn^{2+} concentration dependence of transport. Initial velocities were derived from individual traces
914 of experiments displayed in **A**, the solid line shows the fit to a Michaelis–Menten equation with
915 an apparent K_m of 13.5 μM. (**C**) Mn^{2+} transport in presence of Ca^{2+}. Data display mean of 2 to 7
916 experiments from 2 independent reconstitutions, except for the measurement without divalent ions
917 (0/0, green, mean of 2 experiments). (**D**) Mn^{2+} transport into EcoDMT proteoliposomes in presence
918 of Mg^{2+}. Data display mean of 3 (0/0, green), 4 (50/0, blue) and 9 experiments (50/500, orange
919 and 50/2000, red) from 3 independent reconstitutions. (**E**) Mn^{2+} transport into proteoliposomes
920 containing the EcoDMT mutant M235A. Data display mean of 8 experiments from 3 independent
921 reconstitutions. (**F**) Inhibition of Mn^{2+} transport in the mutant M235A by Ca^{2+} (3 experiments from
922 3 independent reconstitutions). (**G**) Mn^{2+} concentration dependence of transport into M235A
923 proteoliposomes. For Mn^{2+}, initial velocities were derived from individual traces of experiments
924 displayed in **E**, for Mn^{2+} in presence of 2mM Ca^{2+}, data show mean of 3 experiments from 3
925 independent reconstitutions. The solid lines are fits to a Michaelis–Menten equation with apparent
926 K_m of 41 μM (Mn^{2+}) and 107 uM (Mn^{2+} in presence of 2mM Ca^{2+}). (**H**) Ca^{2+}-transport into M235A
927 proteoliposomes assayed with the fluorophore Fura-2. Data display mean of 3 experiments from 3
928 independent reconstitutions. (**I**) Mn^{2+} transport in presence of Mg^{2+}. Data display mean of 6
929 experiments from 3 independent reconstitutions. (**J**) Mn^{2+} transport into proteoliposomes
930 containing the EcoDMT triple mutant M235A/N54G/A232T. Data display mean of 3 experiments
931 from 3 independent reconstitutions. (**K**) Inhibition of Mn^{2+} transport in the mutant
932 M235A/N54G/A232T by Mg^{2+} (6 experiments from 3 independent reconstitutions). (**L**) Mn^{2+}
933 concentration dependence of transport into M235A/N54G/A232T proteoliposomes. For Mn^{2+},

934 initial velocities were derived from individual traces of experiments displayed in **J**, for Mn^{2+} in
935 presence of 2mM Mg^{2+}, data show mean of 3 (without Mg^{2+}, red) and 6 experiments (with Mg^{2+},
936 blue) from 3 independent reconstitutions. The solid lines are fits to a Michaelis–Menten equation
937 with apparent K_m of 31 μM (Mn^{2+}) and 38 μM (Mn^{2+} in presence of 2mM Mg^{2+}). **A, C, D, E, F, I,**
938 **J, K** Uptake of Mn^{2+} was assayed by the quenching of the fluorophore calcein trapped inside the
939 vesicles. **A, C, D, E, F, H, I, J, K** Averaged traces are presented in unique colors. Fluorescence is
940 normalized to the value after addition of substrate (t=0). Applied ion concentrations are indicated.
941 **A-L**, Data show mean of the indicated number of experiments, Errors are s.e.m.

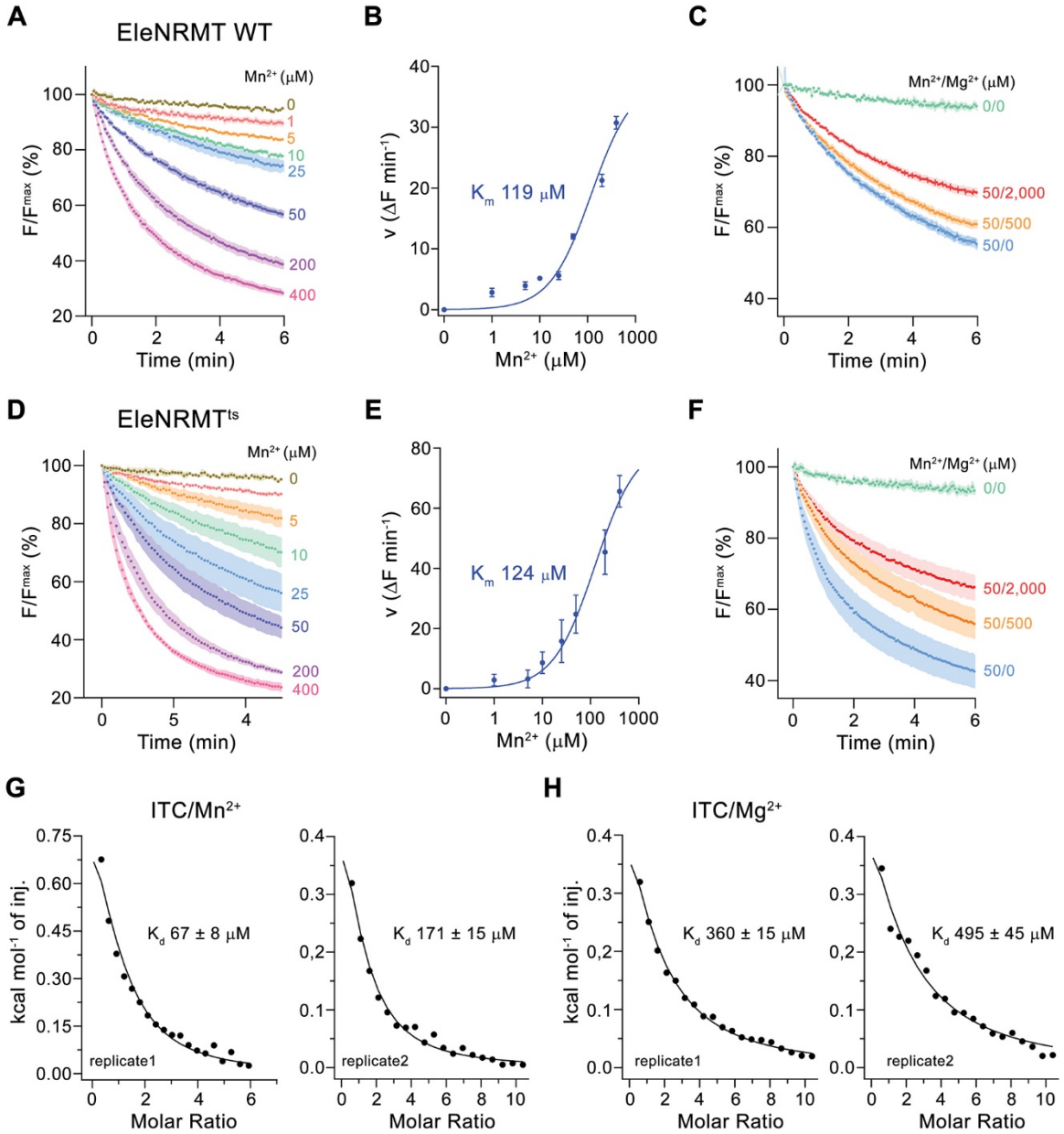

Figure 3. Transport properties of EleNRMT. (**A**) EleNRMT mediated Mn^{2+} transport into proteoliposomes. Data display mean of 3 experiments from 2 independent reconstitutions. (**B**) Mn^{2+} concentration dependence of transport. Initial velocities were derived from individual traces of experiments displayed in **A**, the solid line shows the fit to a Michaelis–Menten equation with an apparent K_m of 119 µM. (**C**) Mn^{2+} transport in presence of Mg^{2+}. Data display mean of 3 (0/0, green), 6 (50/0, blue), 5 (50/500, orange) and 9 (50/2000, red) experiments from 2 independent

949 reconstitutions. (**D**) Mn^{2+} transport into proteoliposomes mediated by the thermostabilized mutant
950 EleNRMT^{ts}. Data display mean of 4 experiments from 2 independent reconstitutions, except for
951 the measurement with 25 µM Mn^{2+} (mean of 3 experiments). (**E**) Mn^{2+} concentration dependence
952 of transport. Initial velocities were derived from individual traces of experiments displayed in **D**,
953 the solid line shows the fit to a Michaelis–Menten equation with an apparent K_m of 124 µM. (**F**)
954 Mn^{2+} transport in presence of Mg^{2+}. Data display mean of 4 (0/0, green), 9 (50/0, blue), 11 (50/500,
955 orange) and 8 (50/2000, red) experiments from 2 independent reconstitutions. **A, C, D, F**. Uptake
956 of Mn^{2+} was assayed by the quenching of the fluorophore calcein trapped inside the vesicles.
957 Averaged traces are presented in unique colors. Fluorescence is normalized to the value after
958 addition of substrate (t=0). Applied ion concentrations are indicated. **A-F**, Data show mean of the
959 indicated number of experiments, Errors are s.e.m.. **G-H**, Binding isotherms obtained from
960 isothermal titrations of Mn^{2+} (**G**) and Mg^{2+} (**H**) to EleNRMT^{ts}. The data shown for two biological
961 replicates per condition was fitted to a model assuming a single binding site with the binding
962 isotherm depicted as solid line. Errors represent fitting errors.

963

964 **Figure supplement 1.** EleNRMT sequence and topology

965 **Figure supplement 2.** Stabilization and biochemical characterization of EleNRMT.

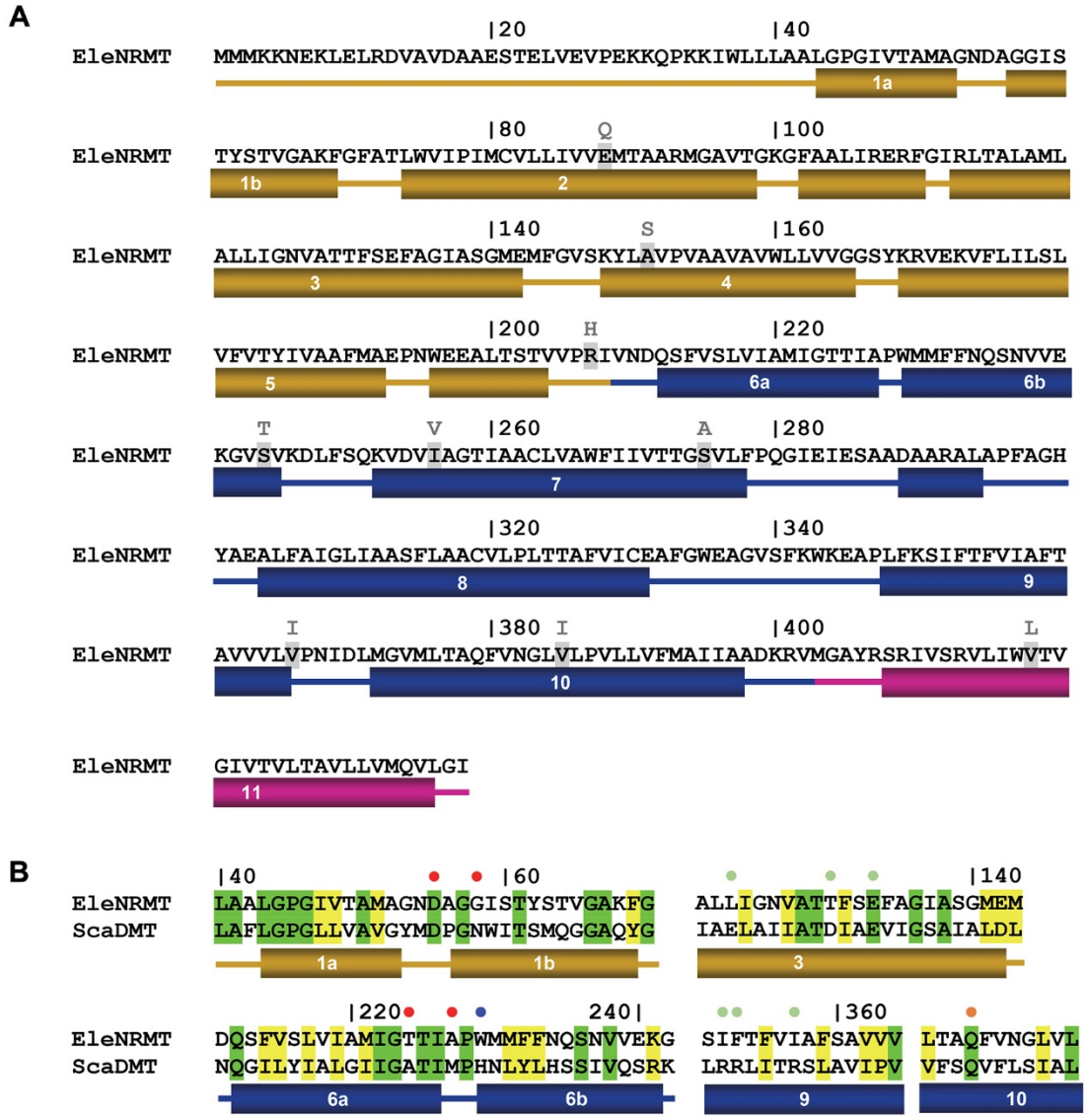

Figure 3—figure supplement 1. EleNRMT sequence and topology. (**A**) Sequence of EleNRMT (NCBI: WP_009305646.1) with secondary structure elements indicated below. Residues mutated in the thermostabilized EleNRMTts are highlighted with replacements shown on top. (**B**) Comparison of functionally relevant regions of EleNRMT and the Mn^{2+} transporter ScaDMT (Uniprot: A0A4U9TNH6) with secondary structure elements shown below. Dots indicate ion binding site (red), a residue interacting with the ion in an occluded state (orange) and positions relevant for H^{+} transport in NRAMPs on α6 (blue) and α3, 9 (green).

974

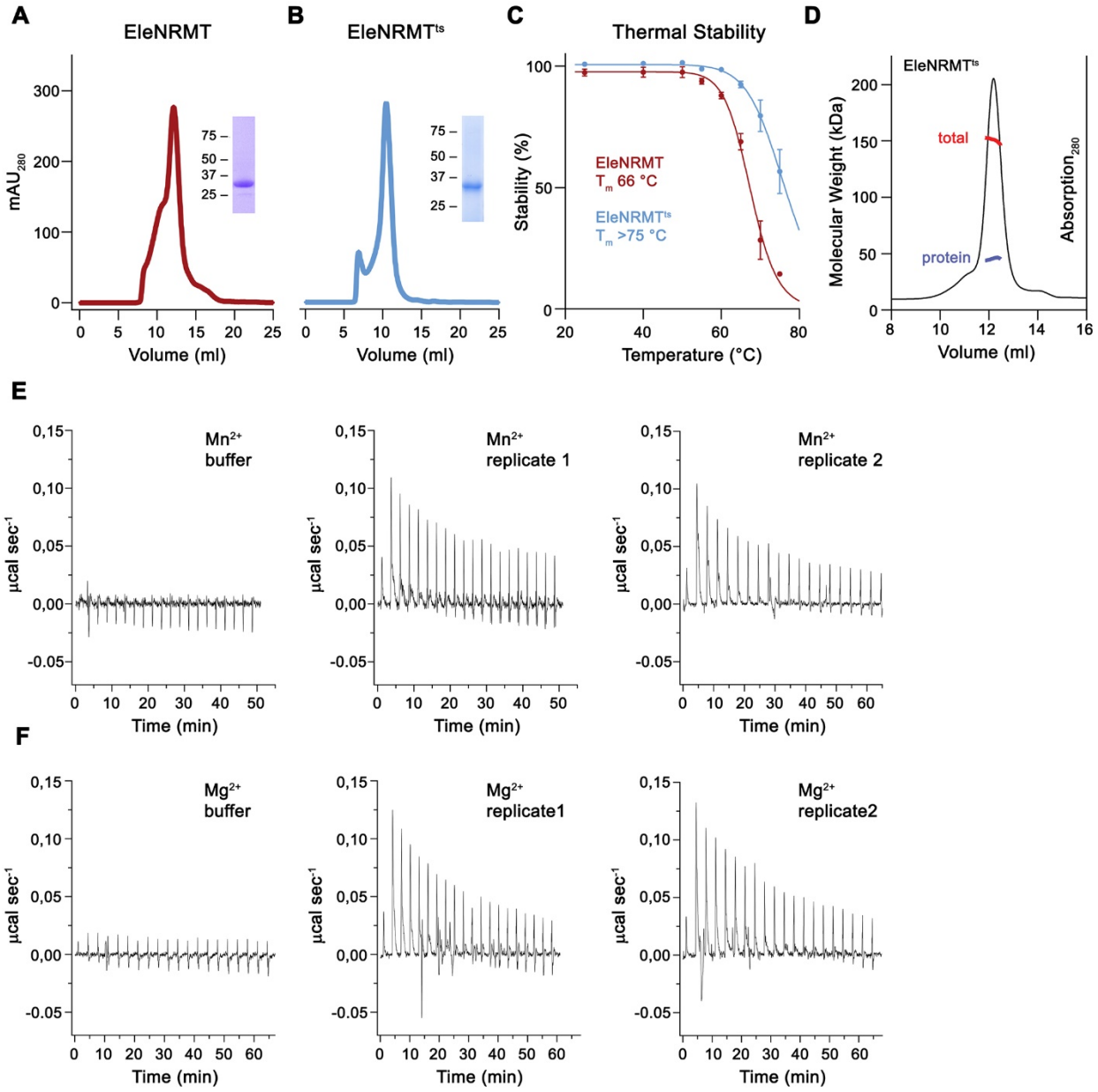

975

976 **Figure 3—figure supplement 2.** Stabilization and biochemical characterization of EleNRMT. Gel
977 filtration profiles on a Superdex 200 column of WT EleNRMT (**A**) and the thermostabilized
978 construct of ElenRMT^{ts} (**B**). Insets show SDS-PAGE gel of peak fractions with molecular weight
979 marker indicated (kDa). (**C**) Thermal stability assay of EleNRMT and EleNRMT^{ts}. Data show

980 averages of four technical replicates, errors are s.e.m.. (**D**) SEC/MALS experiment of purified
981 EleNRMT^{ts} with obtained molecular weight corresponding to a monomeric transporter (measured
982 molecular weight of 45.6 kDa versus theoretical molecular weight of 46.9 kDa). Thermograms of
983 Mn^{2+} (**E**) and Mg^{2+} (**F**) binding to EleNRMT^{ts} obtained from isothermal titration calorimetry
984 experiments shown in Figure 3G, H. E, F Panels show titration against buffer (left) and traces of
985 two biological replicates (center, right)

986

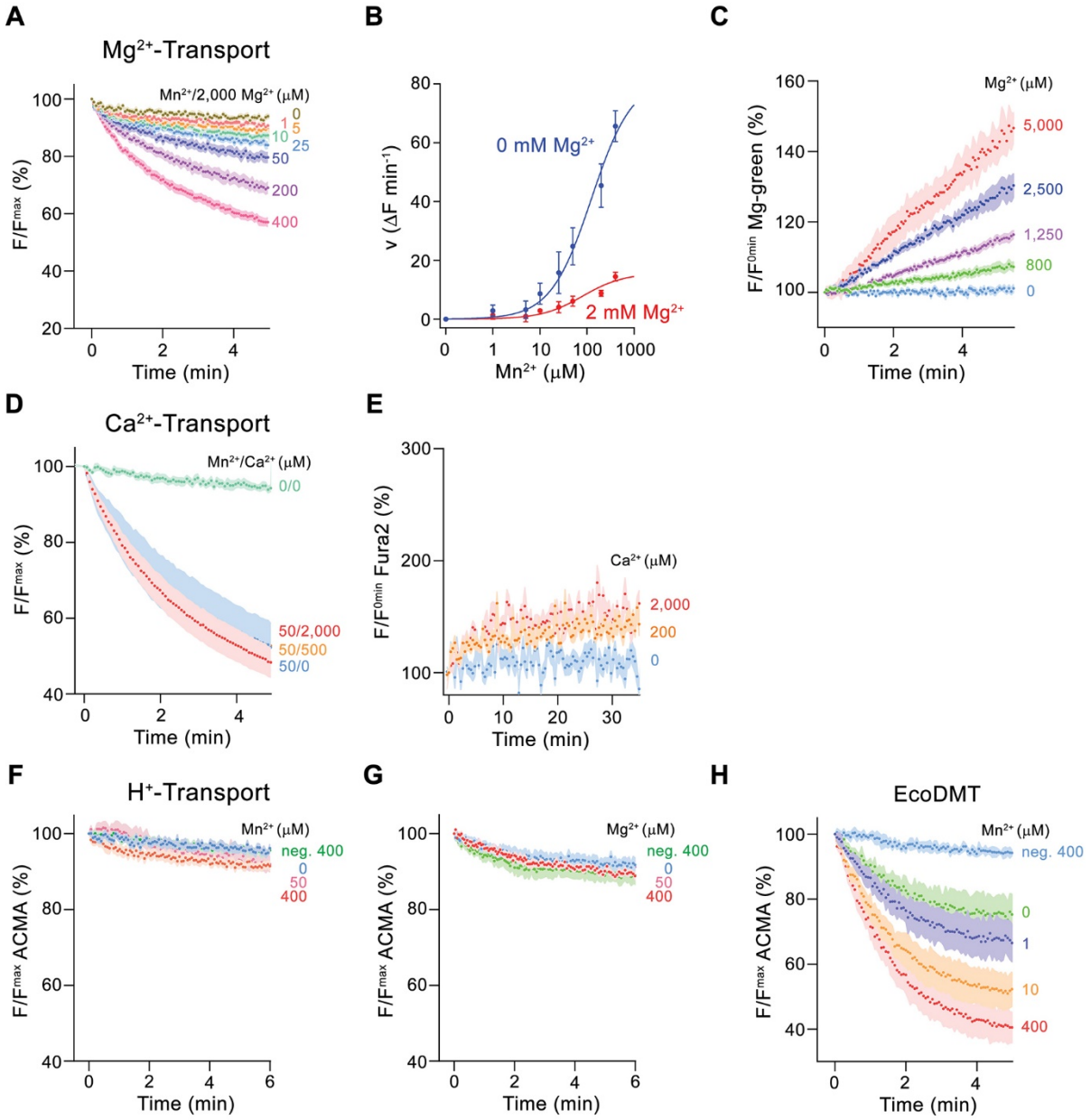

Figure 4. Ion selectivity and substrate coupling. (**A-E**) Metal ion transport by EleNRMT^{ts}. (**A**) EleNRMT^{ts} mediated Mn^{2+} transport into proteoliposomes in presence of 2 mM Mg^{2+}. Data display mean of 8 experiments from 3 independent reconstitutions, except for the measurement with 200 µM Mn^{2+} (mean of 7 experiments). (**B**) Mn^{2+} concentration dependence of transport into EleNRMT^{ts} proteoliposomes. For Mn^{2+}, data are as displayed in Figure 3E, for Mn^{2+} in presence

993 of 2mM Mg^{2+}, initial velocities were derived from individual traces of experiments displayed in
994 **A**. The solid lines are fits to a Michaelis–Menten equation. (**C**) Mg^{2+}-transport into EleNRMT^{ts}
995 proteoliposomes assayed with the fluorophore Magnesium Green. Data display mean of 5 (0 µM
996 Mg^{2+}), 8 (800 µM and 1250 µM Mg^{2+}), 4 (2500 µM Mg^{2+}) and 3 (5000 µM Mg^{2+}) experiments
997 from 2 independent reconstitutions. (**D**) Mn^{2+} transport in presence of Ca^{2+}. Data display mean of
998 4 to 11 experiments from 3 independent reconstitutions. **A, D** Uptake of Mn^{2+} was assayed by the
999 quenching of the fluorophore calcein trapped inside the vesicles. (**E**) Ca^{2+}-transport into
1000 EleNRMT^{ts} proteoliposomes assayed with the fluorophore Fura-2. Data display mean of 3 to 12
1001 experiments from 2 independent reconstitutions. The small increase of the fluorescence at high
1002 Ca^{2+} concentrations is likely from non-specific leak into proteoliposomes. **F-H** Assay of H^+
1003 transport with the fluorophore ACMA. Experiments probing metal ion coupled H^+ transport into
1004 proteoliposomes containing EleNRMT^{ts} upon addition of Mn^{2+} (8 experiments from 2 independent
1005 reconstitutions) (**F**) and Mg^{2+} (8 experiments from 2 independent reconstitutions) (**H**) do not show
1006 any indication of H^+ transport. Mn^{2+} coupled H^+ transport into EcoDMT proteoliposomes (3
1007 experiments from 3 independent reconstitutions and for the negative control (no protein, 400 µM
1008 Mn^{2+}), 4 measurements) is shown for comparison (**I**). **A, C-H** Averaged traces are presented in
1009 unique colors. Fluorescence is normalized to the value after addition of substrate (t=0). Applied
1010 ion concentrations are indicated. **A-H**, Data show mean of the indicated number of experiments,
1011 Errors are s.e.m.

1012

1013 **Figure supplement 1.** Nanobody selection.

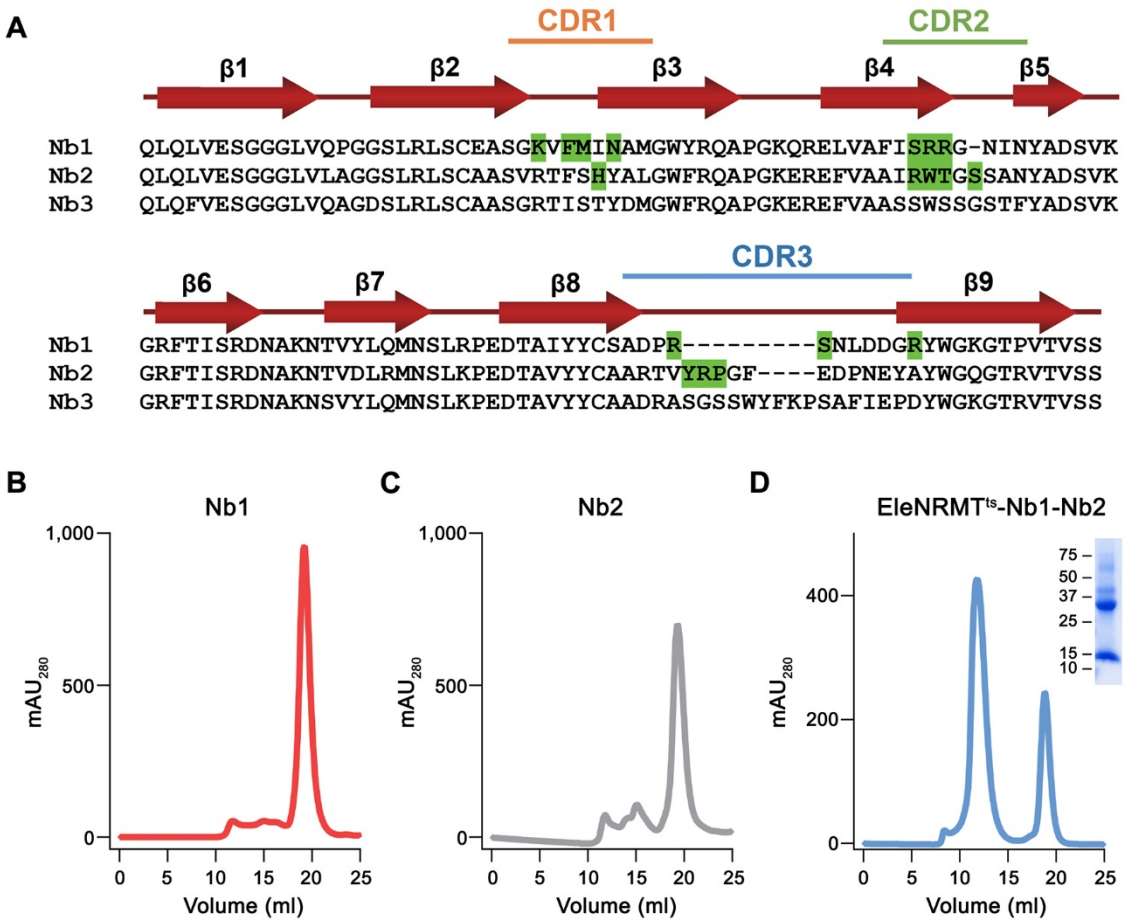

1014

1015 **Figure 4—figure supplement 1.** Nanobody selection. (**A**) Sequence alignment of the three
1016 EleNRMT binders Nb1-Nb3. Secondary structure is shown above. The location of complementary
1017 determining regions (CDRs) are indicated, residues in Nb1 and Nb2 making contacts with
1018 EleNRMT^{ts} are highlighted in green. SEC profiles of purified (**B**) Nb1, (**C**) Nb2, and (**D**) the
1019 EleNRMT^{ts}-Nb1,2 complex assembled with a stoichiometric excess of both nanobodies. Inset
1020 shows SDS-PAGE gel with molecular weights (kDa) indicated.

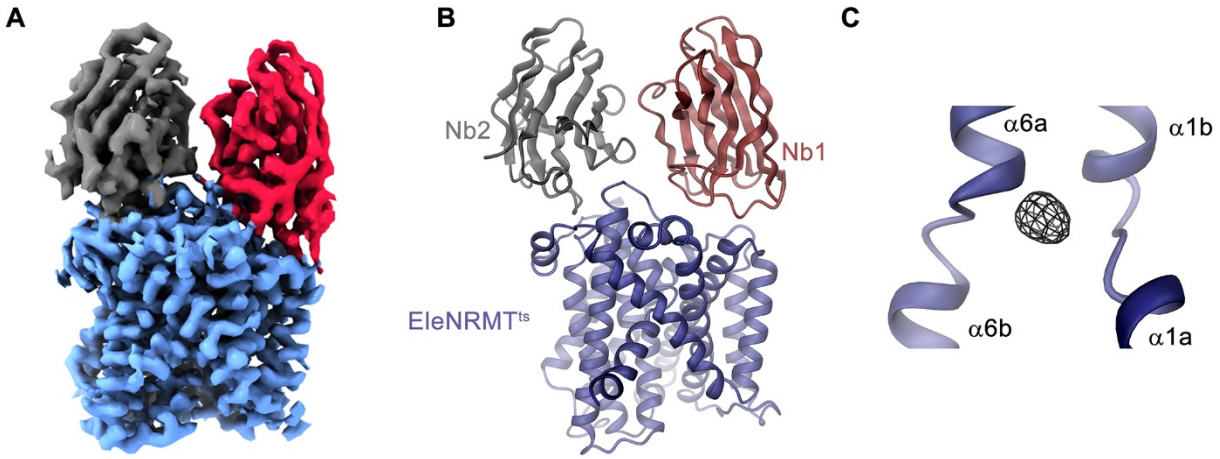

1021

1022 **Figure 5.** Structural characterization of EleNRMT^{ts} by Cryo-EM and X-ray crystallography. (**A**)
1023 Cryo-EM density (contoured at 5 σ) of EleNRMT^{ts} in complex with Nb1 and Nb2 at 3.5 Å viewed
1024 from within the membrane with the extracellular side on top and (**B**), ribbon representation of the
1025 complex in the same view. Proteins are shown in unique colors. (**C**) Anomalous difference density
1026 of Mn^{2+} obtained from the crystal structure of the EleNRMT^{ts}-Nb1-Nb2 complex (calculated at 5
1027 Å and displayed as black mesh contoured at 4.5 σ). Model of EleNRMT^{ts} encompassing the
1028 unwound center of helices α1 and α6 is shown as ribbon.

1029

1030 **Figure supplement 1.** Cryo-EM reconstruction of the EleNRMT^{ts}-nanobody complex.

1031 **Figure supplement 2.** Cryo-EM reconstruction of EleNRMT^{ts}-nanobody in presence of Mg^{2+}.

1032 **Figure supplement 3.** Cryo-EM densities of EleNRMT^{ts}-nanobody complexes.

1033 **Figure supplement 4.** Nanobody interfaces.

1034 **Figure supplement 5.** X-ray structures of EleNRMT^{ts}-nanobody complexes in presence of Mg^{2+}
1035 and Mn^{2+}.

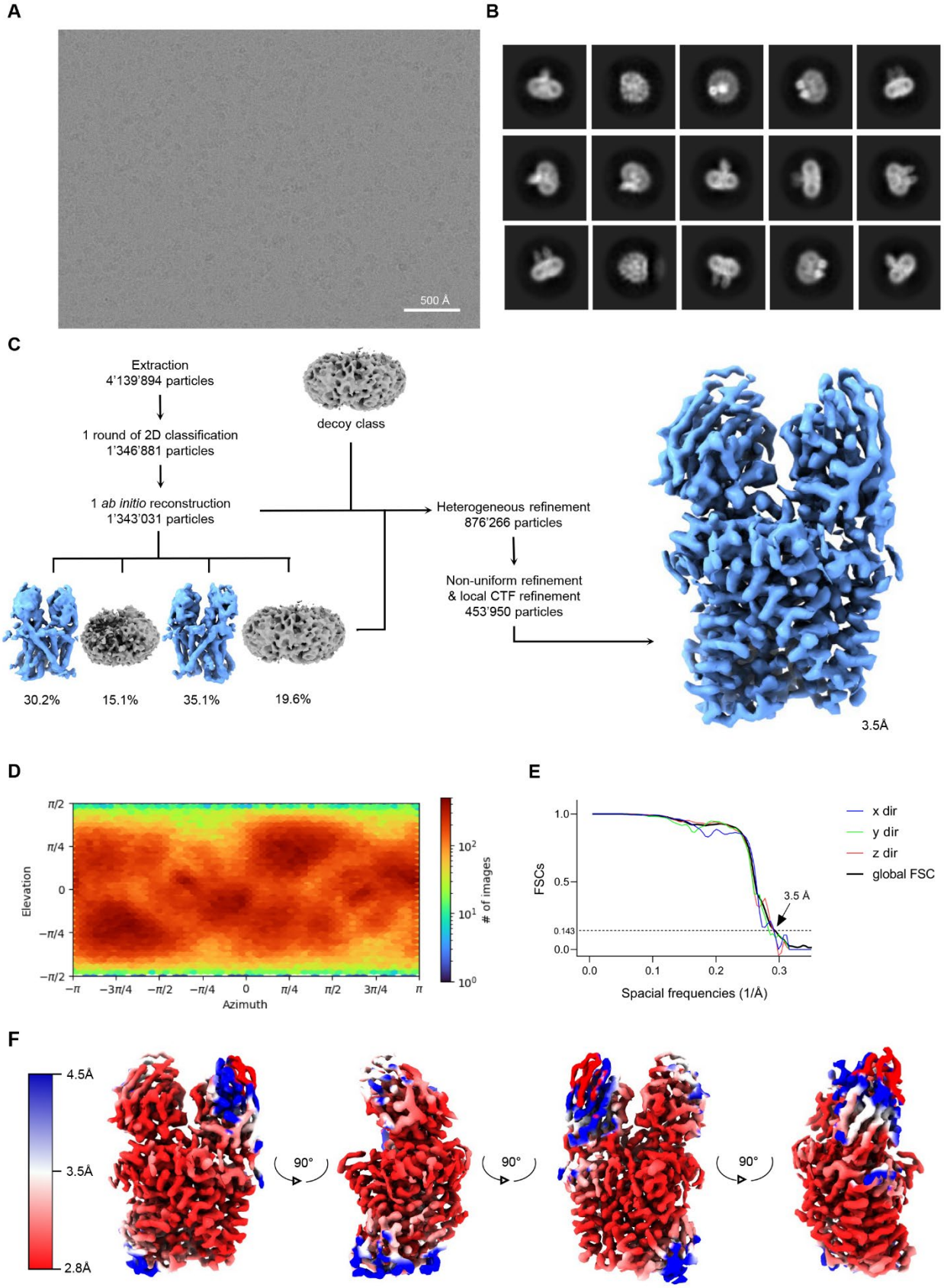
A
500 Å
B
C
Extraction
4'139'894 particles
1 round of 2D classification
1'346'881 particles
1 ab initio reconstruction
1'343'031 particles
decoy class
Heterogeneous refinement
876'266 particles
Non-uniform refinement
& local CTF refinement
453'950 particles
30.2%
15.1%
35.1%
19.6%
3.5Å
D
Elevation
Azimuth
# of images
E
FSCs
Spacial frequencies (1/Å)
x dir
y dir
z dir
global FSC
3.5 Å
0.143
F
4.5Å
3.5Å
2.8Å
90°
90°
90°

1036

1037 **Figure 5—figure supplement 1.** Cryo-EM reconstruction of the EleNRMT^{ts}-nanobody complex.
1038 (**A**) Representative micrograph (out of a total of 22 117 images) of the complex acquired with a
1039 Titan Krios G3i microscope equipped with a K3 camera. (**B**) 2D class averages of the EleNRMT^{ts}-
1040 Nb1-Nb2 dataset. (**C**) Data processing workflow. After extraction and one round of 2D
1041 classification, a single *ab initio* reconstruction with four classes was performed. The particle
1042 distribution is indicated in %. The two most promising classes, together with a decoy class were
1043 subjected to nine rounds of heterogeneous refinement. Non-uniform (NU) refinement, local CTF-
1044 refinement and a second round of NU-refinement with C1 symmetry yielded a map at a resolution
1045 of 3.5 Å. (**D**) Angular distribution of particle orientations. The heatmap displays the number of
1046 particles for a given viewing angle. (**E**) Directional and global FSC plots. The global FSC is shown
1047 in black. Dashed line indicates 0.143 cut-off and the resolution at which the FSC curve drops below
1048 0.143 is indicated. The directional FSC curves providing an estimation of anisotropy of the dataset
1049 are shown for directions x, y, and z. (**F**) Final 3D reconstruction of the EleNRMT^{ts}-Nb1-Nb2
1050 complex in indicated orientations, colored according to the local resolution, estimated in
1051 cryoSPARC v.3.2.0.

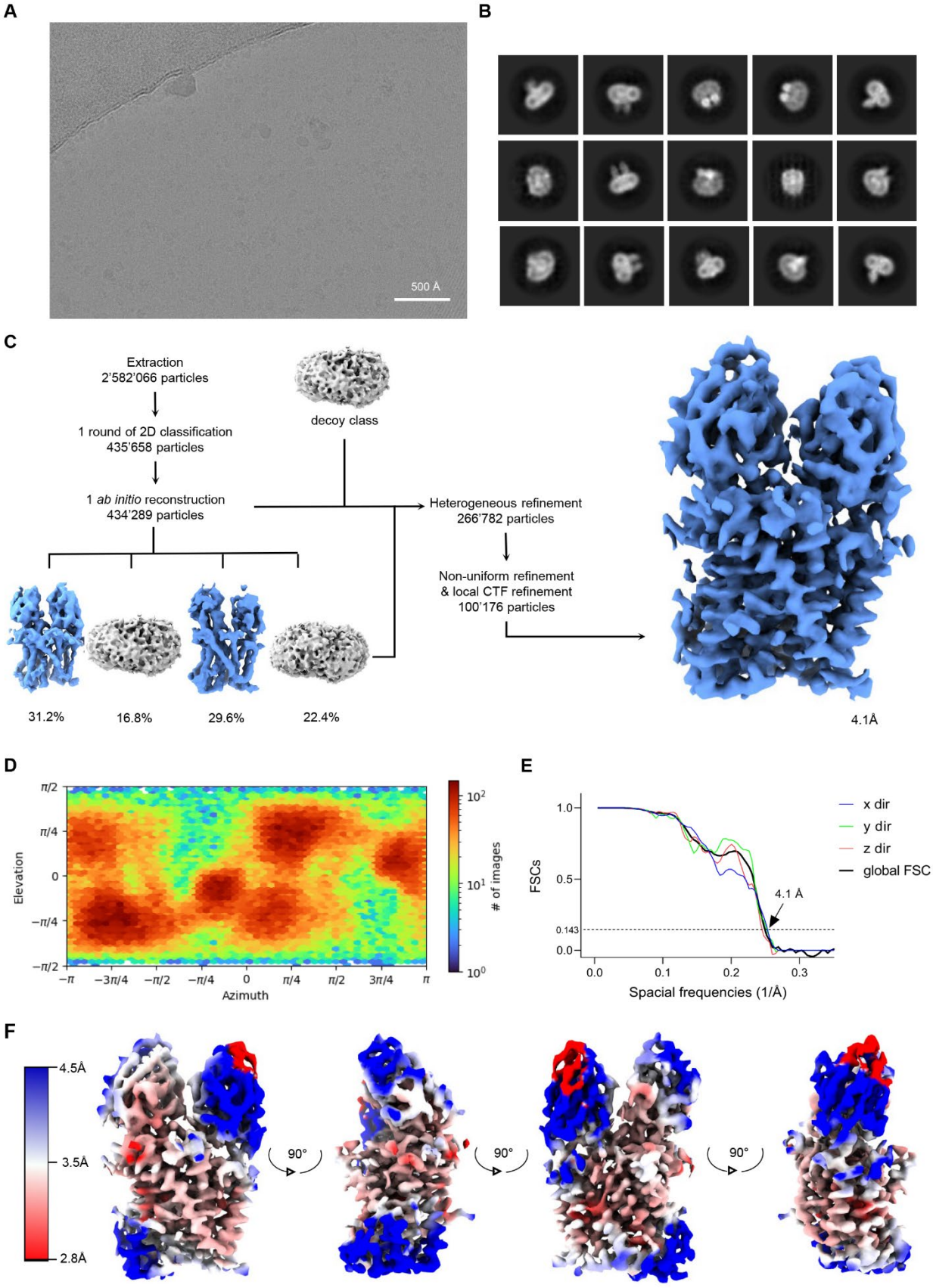
A
500 Å
B
C
Extraction
2'582'066 particles
1 round of 2D classification
435'658 particles
1 ab initio reconstruction
434'289 particles
decoy class
Heterogeneous refinement
266'782 particles
Non-uniform refinement
& local CTF refinement
100'176 particles
31.2%
16.8%
29.6%
22.4%
4.1Å
D
Elevation
Azimuth
# of images
E
FSCs
Spacial frequencies (1/Å)
x dir
y dir
z dir
global FSC
4.1 Å
0.143
F
4.5Å
3.5Å
2.8Å
90°
90°
90°

1052

1053 **Figure 5—figure supplement 2.** Cryo-EM reconstruction of EleNRMT^{ts}-nanobody in presence
1054 of Mg^{2+}. (**A**) Cryo-EM reconstruction of the EleNRMT^{ts}-nanobody complex in presence of Mg^{2+}.
1055 (**A**) Representative micrograph (out of a total of 12 427 images) of the complex acquired with a
1056 Titan Krios G3i microscope equipped with a K3 camera. (**B**) 2D class averages of the EleNRMT^{ts}-
1057 Nb1-Nb2 dataset. (**C**) Data processing workflow. After extraction and one round of 2D
1058 classification, a single *ab initio* reconstruction with four classes was performed. The particle
1059 distribution is indicated in %. The particles from the two most promising classes, together with a
1060 decoy class were subjected to 22 rounds of heterogeneous refinement. Non-uniform (NU)
1061 refinement, local CTF-refinement and a second round of NU-refinement with C1 symmetry
1062 yielded a map at a resolution of 4.1 Å. (**D**) Angular distribution of particle orientations. The
1063 heatmap displays the number of particles for a given viewing angle. (**E**) Directional and global
1064 FSC plots. The global FSC is shown in black. Dashed line indicates 0.143 cut-off and the resolution
1065 at which the FSC curve drops below 0.143 is indicated. The directional FSC curves providing an
1066 estimation of anisotropy of the dataset are shown for directions x, y, and z. (**F**) Final 3D
1067 reconstruction of the EleNRMT^{ts}-Nb1-Nb2 complex in indicated orientations, colored according
1068 to the local resolution, estimated in cryoSPARC v.3.2.0.

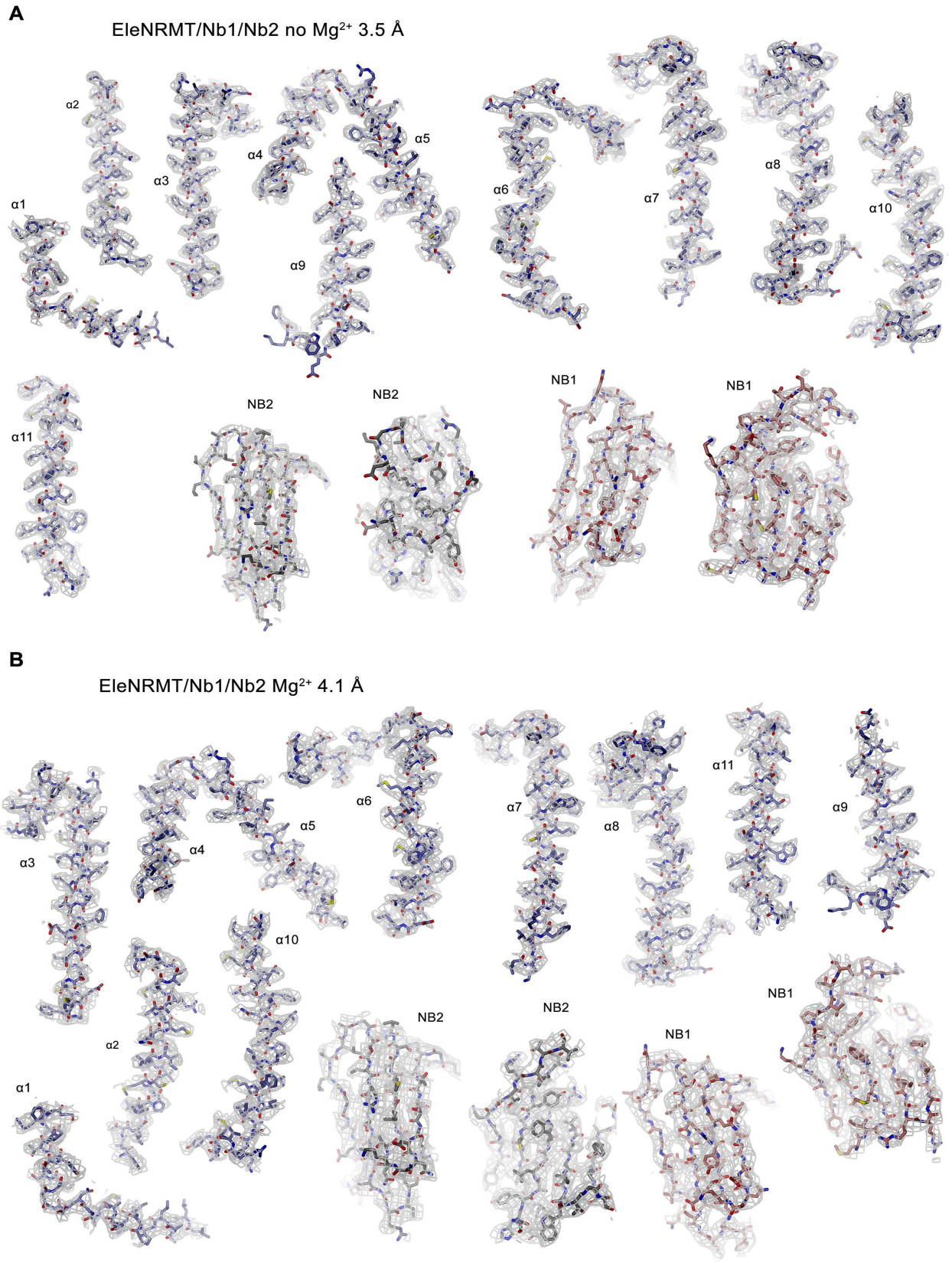
A
EleNRMT/Nb1/Nb2 no Mg2+ 3.5 Å
α1
α2
α3
α4
α5
α6
α7
α8
α9
α10
α11
NB2
NB2
NB1
NB1
B
EleNRMT/Nb1/Nb2 Mg2+ 4.1 Å
α1
α2
α3
α4
α5
α6
α7
α8
α9
α10
α11
NB2
NB2
NB1
NB1

1069

1070 **Figure 5—figure supplement 3.** Cryo-EM densities of EleNRMT-nanobody complexes. (**A**)
1071 EleNRMT^{ts}-nanobody complex in absence of Mg^{2+} at 3.5 Å. Electron density (contoured at 6σ,
1072 grey mesh) is shown superimposed on indicated protein regions. (**B**) EleNRMT^{ts}-nanobody
1073 complex in presence of Mg^{2+} at 4.1 Å. Electron density (contoured at 6σ, grey mesh) is shown
1074 superimposed on indicated protein regions.

1075

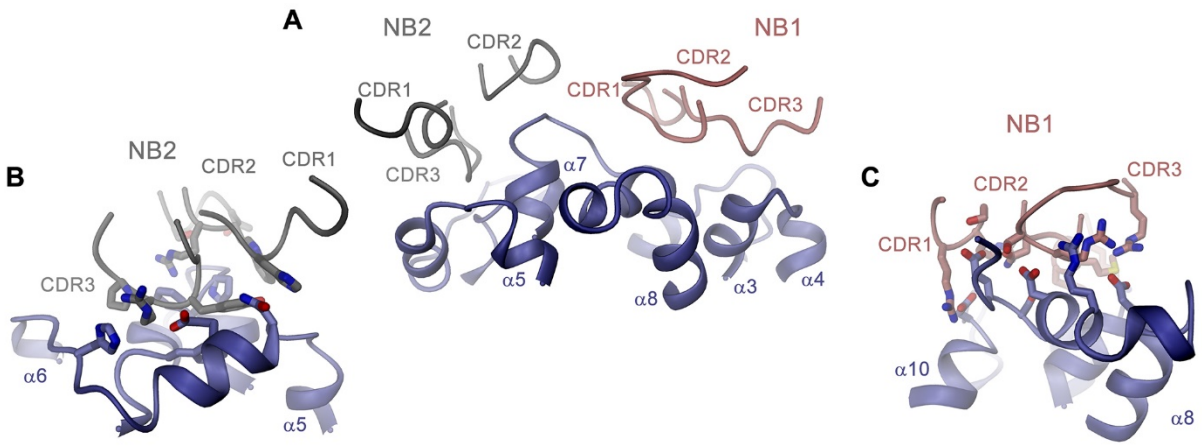

1076

1077 **Figure 5—figure supplement 4.** Nanobody binding interfaces. (**A**) Contact region of EleNRMT^{ts}
1078 and nanobodies Nb1 and Nb2. (**B**) Binding interface of Nb2. (**C**) Binding interface of Nb1. **C**, **D**,
1079 Side chains of residues mediating binding interactions between the transporter and the nanobodies
1080 are displayed as sticks. **A-C** Proteins are shown as ribbons with respective regions labeled.

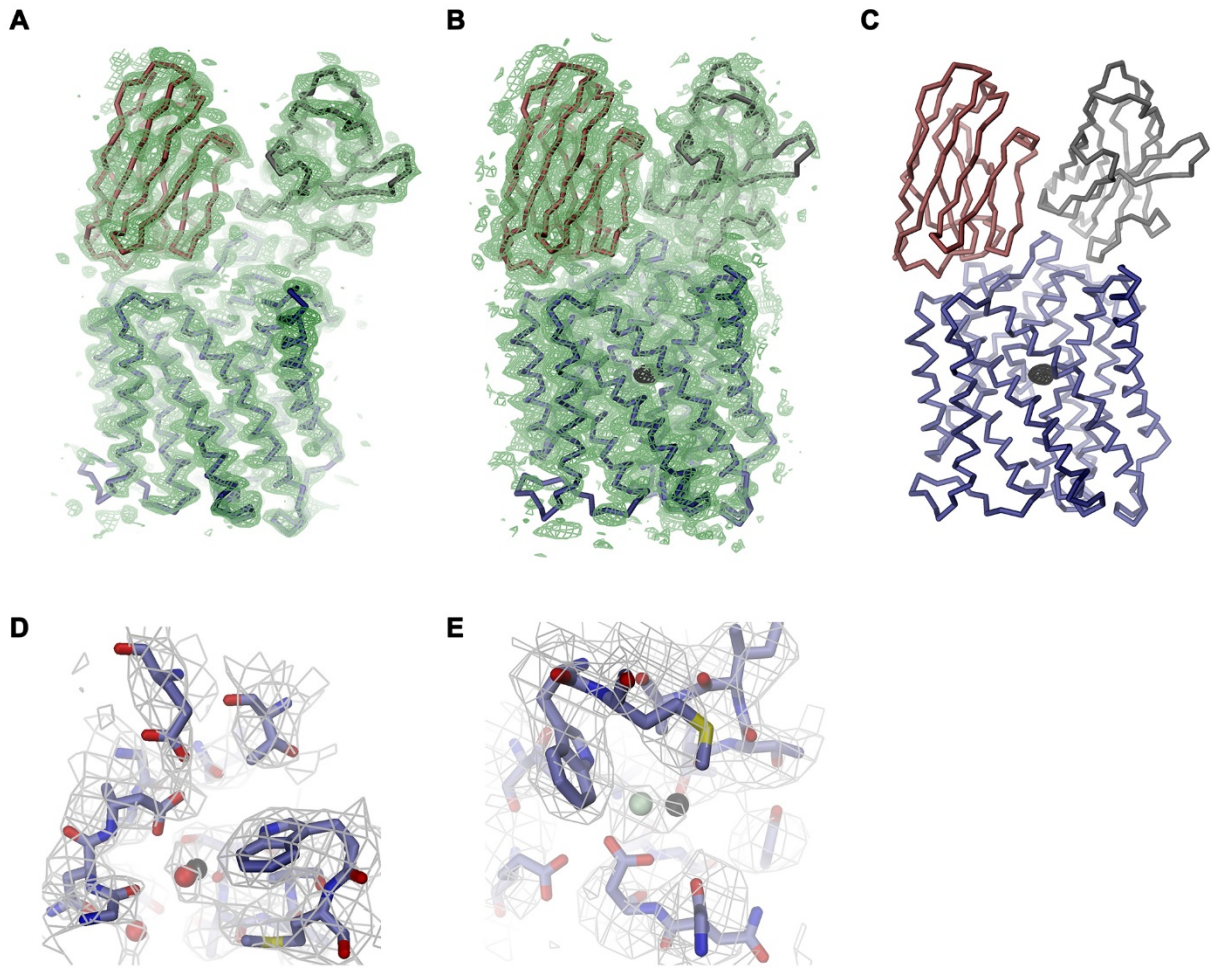

1081

1082 **Figure 5—figure supplement 5.** X-ray structures of EleNRMT-nanobody complexes in presence
1083 of Mg^{2+} and Mn^{2+}. (**A**) Structure of the EleNRMT^{ts}-Nb1-Nb2 complex in Mg^{2+} at 4.1 Å (**B**)
1084 Structure of the EleNRMT^{ts}-Nb1-Nb2 complex soaked in Mn^{2+} at 4.6 Å. A, B 2Fo-Fc density
1085 (contoured at 1 σ) is shown as green mesh superimposed on the model. B, C, Anomalous difference
1086 electron density (calculated at 6 Å and contoured at 4 σ) from the dataset displayed in B is depicted
1087 as black mesh. A-C, shown is one of two complexes in the asymmetric unit as Cα trace with protein
1088 chains displayed in unique colors. Phases for 2Fo-Fc and anomalous difference density maps were
1089 obtained from molecular replacement using the cryo-EM model improved by constrained minimal
1090 refinement. Residual density in the cryo-EM maps of the EleNRMT^{ts}-Nb1-Nb2 complex in

1091 absence (**D**) and presence of Mg^{2+} (**E**) in vicinity to the Mn^{2+} binding position (indicated by black

1092 sphere). Protein is represented as sticks with water (red) or Mg^{2+} (green) as spheres. Maps are as

1093 displayed in Figure 5—figure supplement 3**.**

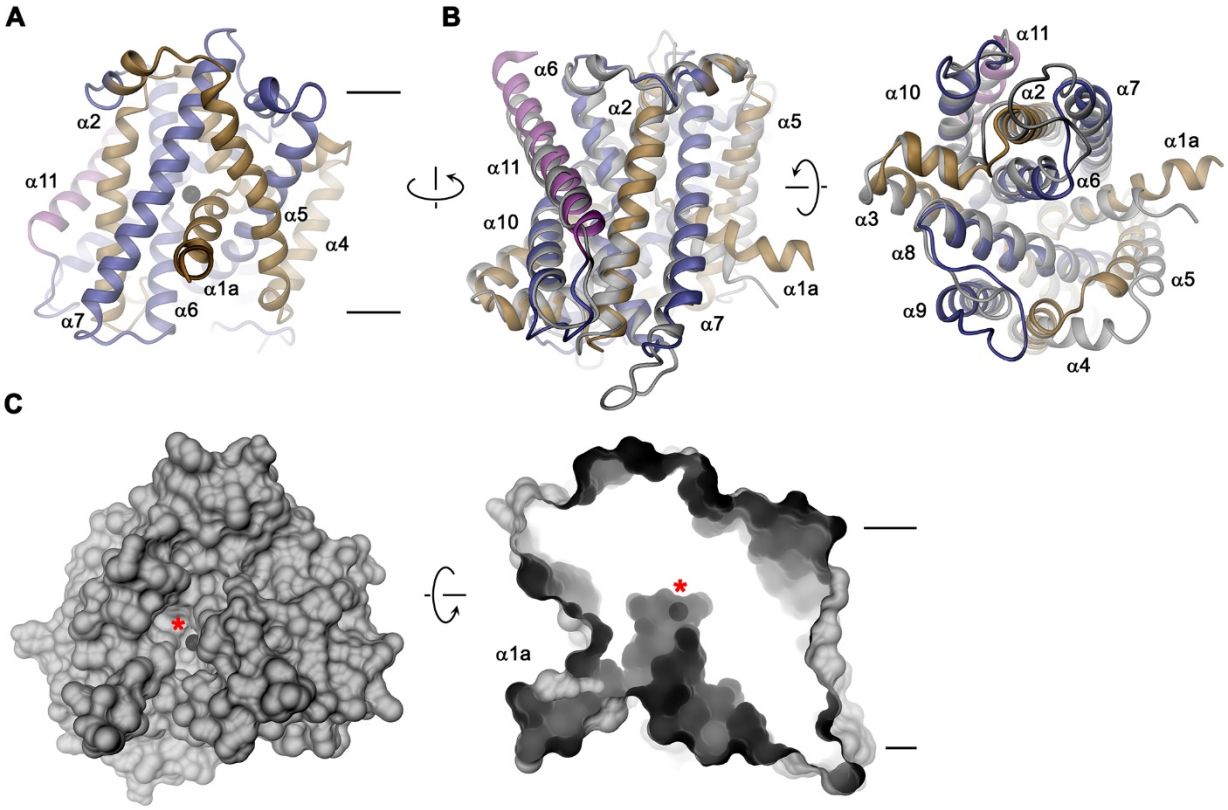

1094

1095 **Figure 6.** EleNRMT structure. (**A**) Ribbon representation of EleNRMT viewed from within the
1096 membrane with α1-α5 colored in beige, α6- α10 in blue and α11 in magenta. the position of a
1097 bound ion is indicated by a black sphere. (**B**) Superposition of EleNRMT and ScaDMT (with
1098 modeled α1a), both showing equivalent inward-open conformations. Ribbon representation of
1099 ScaDMT is shown in grey, the representation of EleNRMT is as in A. (**C**) Surface representation
1100 of EleNRMT. Left, view from the cytoplasm and, right, slice of the surface of EleNRMT viewed
1101 from within the membrane, both showing the aqueous cavity leading to the ion binding site. The
1102 position of a bound ion is represented by a black sphere and with a red asterisk. A-C Selected
1103 helices are labeled. Membrane boundaries (A, C) and relationship between views (A-C) are
1104 indicated.

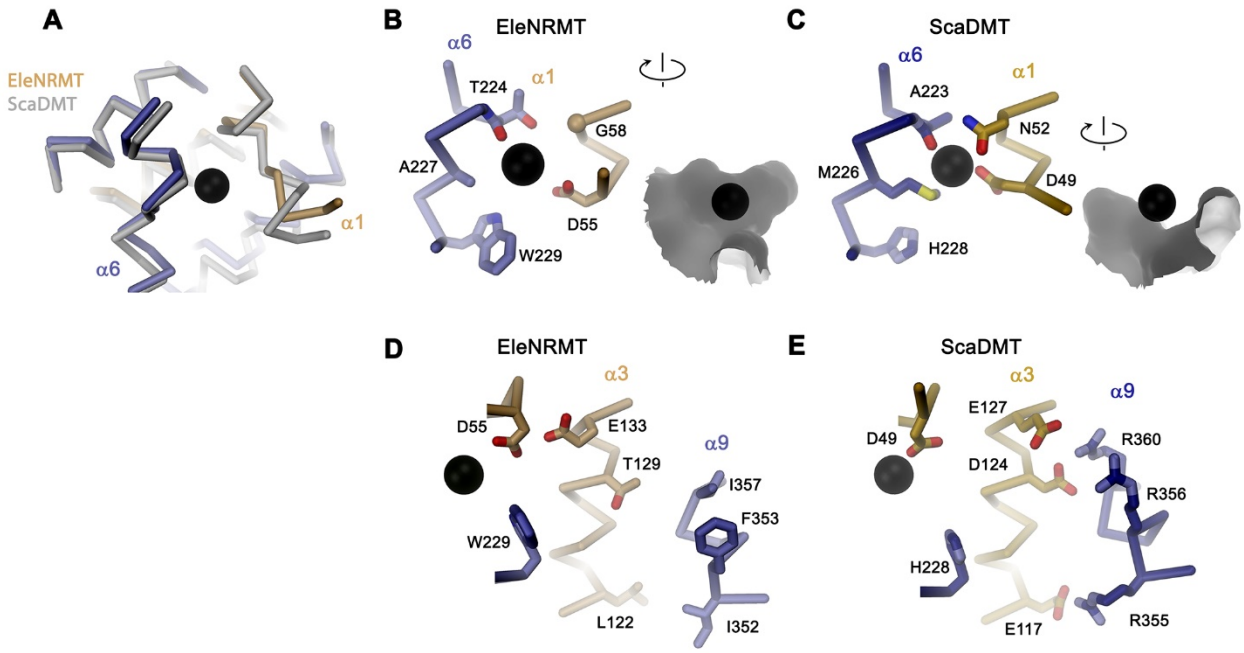

Figure 7. Comparison of regions of functional relevance between EleNRMT and ScaDMT. (**A**) Superposition of the metal ion binding regions of EleNRMT and ScaDMT. The coloring is as in Figure 6B. (**B**) Metal ion binding sites of EleNRMT (**B**) and ScaDMT (**C**). B, C, inset (right) shows molecular surface surrounding the bound ion with indicated relationship. (**D**) Region of EleNRMT on α3 and α9 implicated in proton transport in NRAMPs and corresponding region in ScaDMT (**E**). D, E the bound ion with the conserved binding site Asp on α1 and a residue corresponding to the α6b His in NRAMPs, which was identified as potential H^+ acceptor are shown for reference. A-E The proteins are depicted as Cα-trace, selected residues as sticks. The position of bound metal ions is represented as a black sphere. B-E selected secondary structure elements and residues are indicated.

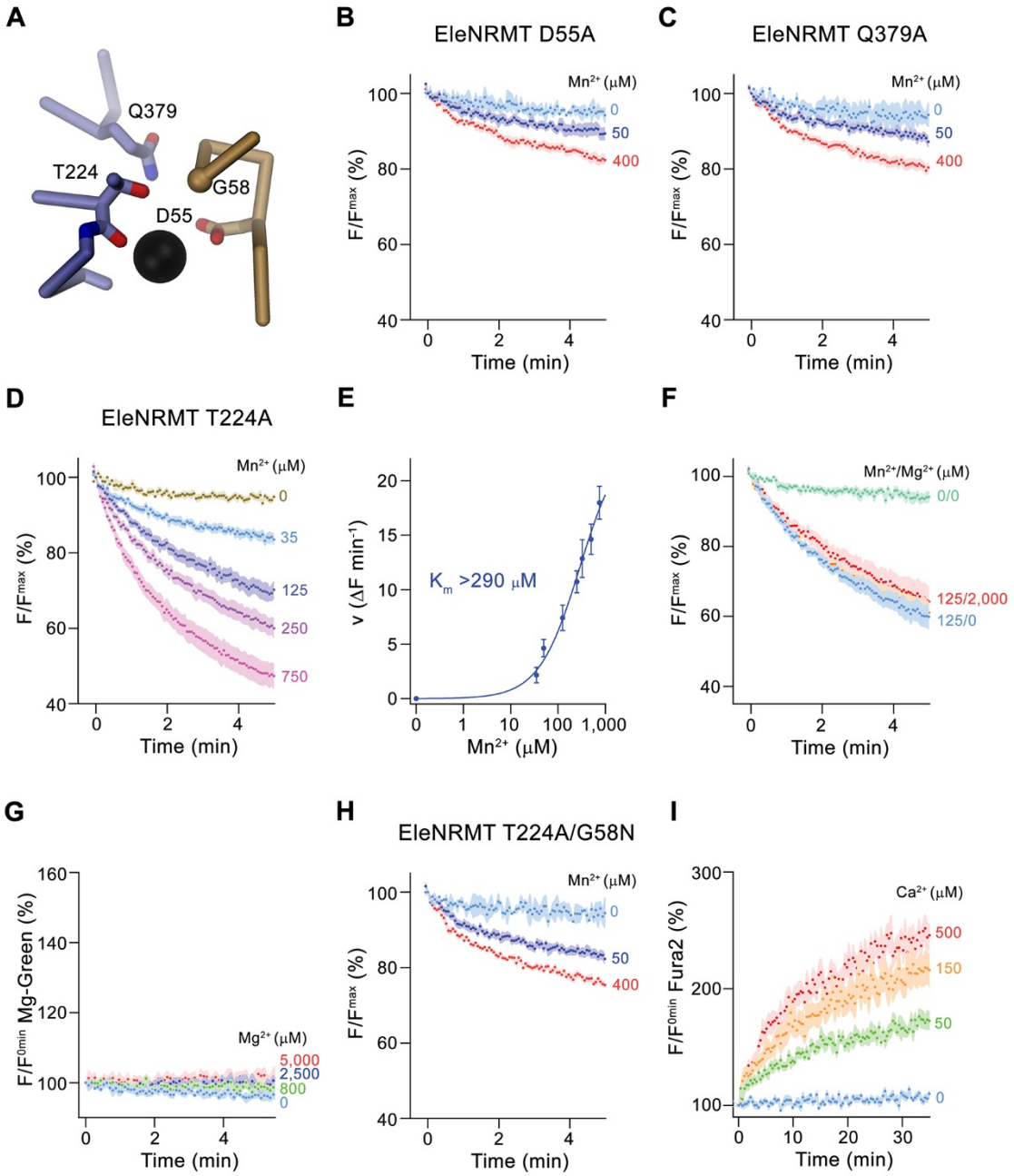

Figure 8. Functional characterization of binding site mutants. (**A**) Model of the ion binding site of EleNRMT with ion (black sphere) showing bound Mn^{2+}. Regions of α1 and α6 are shown as Cα-trace, selected residues coordinating the ion as sticks. (**B-D**) Mn^{2+} transport mediated by EleNRMT^{ts} binding site mutants. (**B**) D55A (2 (0 μM Mn^{2+}), 6 (50 μM Mn^{2+}) and 7 (400 μM

1121 Mn^{2+})experiments from 2 independent reconstitutions), (**C**) Q379A (2 (0 μM Mn^{2+}), 6 (50 μM
1122 Mn^{2+}) and 7 (400 μM Mn^{2+}) experiments from 2 independent reconstitutions), (**D**) T224A (5
1123 experiments from 2 independent reconstitutions). (**E**) Mn^{2+} concentration dependence of transport
1124 of T224A. Initial velocities were derived from individual traces of experiments displayed in **D**, the
1125 solid line shows the fit to a Michaelis–Menten equation with an apparent K_m exceeding 290 μM.
1126 (**F**) Mn^{2+} transport into T224A proteoliposomes in presence of Mg^{2+} (4 experiments from 2
1127 independent reconstitutions). (**G**) Mg^{2+}-transport into T224A proteoliposomes assayed with the
1128 fluorophore Magnesium green (4 experiments from 2 independent reconstitutions). H-I Transport
1129 mediated by the EleNRMT^{ts} binding site mutant T224A/G58N. (**H**) Mn^{2+} transport into
1130 proteoliposomes containing T224A/G58N (2 (0 μM Mn^{2+}), 6 (50 μM Mn^{2+}) and 7 (400 μM Mn^{2+})
1131 experiments from 2 independent reconstitutions). (**I**) Ca^{2+}-transport into T224A/G58N
1132 proteoliposomes assayed with the fluorophore Fura-2 (9 (0 μM Ca^{2+}), 10 (50 μM Ca^{2+}), 11 (150
1133 μM Ca^{2+}) and 10 (500 μM Ca^{2+}) experiments from 2 independent reconstitutions). **B-D, F- H**
1134 Uptake of Mn^{2+} was assayed by the quenching of the fluorophore calcein trapped inside the
1135 vesicles. **B-D, F-I** Averaged traces are presented in unique colors. Fluorescence is normalized to
1136 value after addition of substrate (t=0). Applied ion concentrations are indicated. **B-I**, Data show
1137 mean of the indicated number of experiments, Errors are s.e.m.

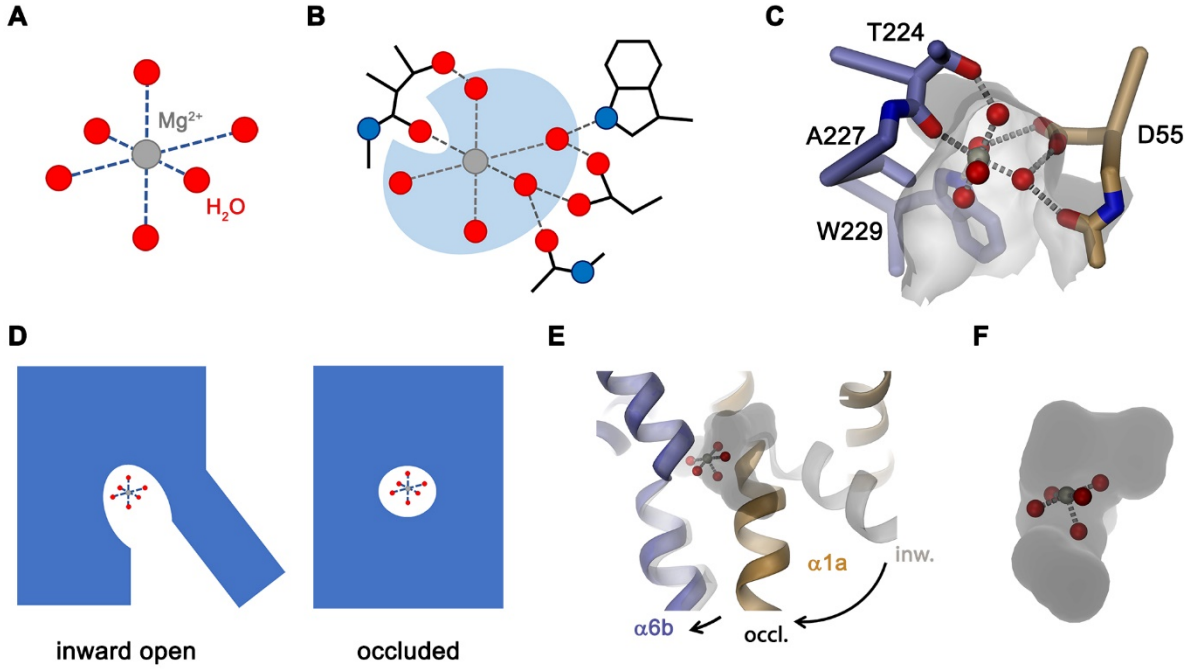

1138

1139 **Figure 9.** Features of Mg^{2+} transport by NRMTs. Schematic depiction of (**A**), the octahedral
1140 coordination of the first hydration shell surrounding a Mg^{2+} ion and (**B**), the same octahedral
1141 coordination within the binding site of a NRMT with five of the six water molecules remaining
1142 bound to the ion and where the bulk of protein interactions with the ion are mediated via
1143 coordinated water. (**C**) Model of Mg^{2+} bound to the site of EleNRMT in the inward-facing
1144 conformation. The coordinates of the hydrated Mg^{2+} were obtained from the high-resolution
1145 structure of the Mg^{2+} transporter MgtE (PDBID 4U9L). The Mg^{2+} ion was placed on the position
1146 of Mn^{2+} obtained from the anomalous difference density defined in the X-ray structure. A single
1147 water molecule with a backbone oxygen atom was removed and the remaining complex was
1148 oriented to maximize interactions of coordinating waters with protein residues. Regions of the
1149 binding site are represented as Cα-trace and selected interacting residues as sticks. The molecular
1150 surface surrounding the binding site of the apo transporter is shown. (**D**) Schematic depiction from
1151 an -inward-facing to an occluded conformation of a NRMT with bound hydrated Mg^{2+} indicated.

1152 (**E**) Approximate model of the transition of EleNRMT from an inward-facing (grey) to an occluded
1153 conformation (colored) that was based on the occluded conformation of DraNRAMP (PDBID:
1154 6C3I). (**F**) Close-up of the modeled binding pocket with bound Mg^{2+}-$5H_2O$ complex. E-F, binding
1155 pocket was calculated from EleNRMT modeled in and occluded conformation.

1156 **Table 1. Cryo-EM data collection, refinement and validation statistics.**

	Dataset 1 EleNRMT-NB (EMDB-) (PDB)	Dataset 2 EleNRMT-NB Mg^{2+} complex (EMDB-) (PDB)
Data collection and processing		
Microscope	FEI Titan Krios	FEI Titan Krios
Camera	Gatan K3 GIF	Gatan K3 GIF
Magnification	130’000	130’000
Voltage (kV)	300	300
Electron exposure (e^{-}/Å^2)	69.725/ 61/ 69.381	69.554
Defocus range (μm)	-1.0 to -2.4	-1.0 to -2.4
Pixel size* (Å)	0.651 (0.3255)	0.651 (0.3255)
Initial number of micrographs (no.)	22117	12427
Initial particle images (no.)	4 139 894	2 582 066
Final particle images (no.)	453 950	100 176
Symmetry imposed	C1	C1
Map resolution (Å)	3.5	4.1
FSC threshold	0.143	0.143
Map resolution range (Å)	2.9-7.0	3.3-8.3
Refinement		
Model resolution (Å)	3.5	4.1
FSC threshold	0.5	0.5
Map sharpening b-factor (Å^2)	-184.4	-159.2
Model vs Map CC (mask)	0.79	0.79
Model composition		
Non-hydrogen atoms	4846	4844
Protein residues	640	640
Ligand	0	1 (Mg)
Water	3	0
B factors (Å2)		
Protein	39.92	44.04
Ligand	0	28.38
Water	22.87	0
R.m.s. deviations		
Bond lengths (Å)	0.003	0.003
Bond angles (°)	0.641	0.652

Validation		
MolProbity score	2.08	2.17
Clashscore	11.93	13.05
Poor rotamers (%)	0	0
Ramachandran plot		
Favored (%)	91.96	90.06
Allowed (%)	8.04	9.94
Disallowed (%)	0	0

*Values in parentheses indicate the pixel size in super-resolution.

1160 **Table 2. X-ray data collection and refinement statistics**

	EleNRMT-Nb complex	EleNRMT-Nb complex Mn^{2+}-soak
Data collection		
Space group	P21	P21
Cell dimensions		
a, *b*, *c* (Å)	93.3, 122.2, 149.1	92.9, 115.9, 149.1
α,*β*,*γ* (°)	90, 107.8, 90	90, 107.6, 90
Wavelength (Å)	1.000	1.896
Resolution (Å)	50-4.1 (4.2-4.1)	50-4.6 (4.7-4.6)
R_{merge}	12.5 (166.8)	15.4 (147.6)
$I / \sigma I$	11.6 (2.4)	10.8 (1.8)
Completeness (%)	99.1 (98.9)	99.8 (99.6)
Redundancy	25.1 (27.1)	14.0 (14.1)
Refinement		
Resolution (Å)	12-4.1	12-4.6
No. reflections	23700	15750
R_{work} / R_{free}	27.1 / 29.6	27.0 / 31.8
No. atoms		
Protein	9536	9536
solvent	6	6
B-factors		
Protein	286.4	272.4
solvent	247.9	288.7
R.m.s deviations		
Bond lengths (Å)	0.005	0.005
Bond angles (°)	0.66	0.66

1161 Values in parentheses are for highest-resolution shell.
1162